

Master's Thesis

# 3D-TV Rendering from Multiple Cameras

**Thesis committee:**

Prof. dr. ir. Jan Biemond

Dr. C.P. Botha

Dr. Emile A. Hendriks

Dr. ir. Andre Redert

|                   |   |
|-------------------|---|
| Author            | Anastasia Manta                             |
| Email             | amantamio@hotmail.com                       |
| Student number    | 1337424                                     |
| Thesis supervisor | Dr. Emile A.Hendriks<br>Dr.ir. Andre Redert |
| Date              | November 12, 2008                           |



**Preface**

This thesis is the final work of my Master study at the Information and Communication Theory group, Faculty of Electrical Engineering, Mathematics and Informatics, at Delft University of Technology. It serves as documentation of my work during the graduation, which has been made from February 2008 until November 2008. This graduation has been preceded by a research assignment on Multiview Imaging and 3DTV during the period October 2007 - January 2008.

Anastasia Manta

Delft, November 2008

**Acknowledgements**

One year ago, deciding my thesis topic was not an easy task. There were so many things in my mind and a wide range of different interesting topics to choose from. One year after, I would sincerely like to thank my supervisors, Emile and Andre, for being really good teachers. I would like to thank them for being supportive and creative, for our fruitful discussions and for teaching me the way to overcome problems and come up with new fresh ideas. It was a pleasure working with them.

The ICT group provided a friendly and pleasant environment to work. I would like to thank everybody who contributed to the nice atmosphere of the group.

Finally, I have to admit that spending two years in TUDelft was an unexpectedly nice experience. I am grateful to all the people that were part of my experience. Especially my family in Greece, my friends, the old and the new ones.



**Contents**

- 1. Introduction ..... - 6 -**
  - a. Three - Dimensional Television (3D TV) ..... - 6 -**
  - b. Three-Dimensional Television; a chain of processes ..... - 7 -**
  - c. Problem Statement ..... - 8 -**
- 2. Related work ..... - 10 -**
  - a. Model-based rendering (MBR) – rendering with explicit geometry..... - 10 -**
  - b. Image-based rendering (IBR) – rendering with no geometry ..... - 15 -**
  - c. Hybrid techniques – rendering with implicit geometry ..... - 18 -**
  - d. Compatibility with 3DTV applications..... - 25 -**
- 3. Rendering ..... - 26 -**
  - a. Basic approach..... - 27 -**
  - b. Weighted approach ..... - 32 -**
  - c. Outlier removal approach..... - 35 -**
- 4. Experimental setup..... - 43 -**
- 5. Evaluation ..... - 46 -**
- 6. Discussion and Future work ..... - 52 -**
  - b. Future Research..... - 53 -**
- 7. Appendix ..... - 54 -**
  - A. Results..... - 54 -**
  - B. Clustering experiment..... - 60 -**
  - C. Depth maps..... - 64 -**
  - D. Mean Shift algorithm ..... - 65 -**
- 8. References ..... - 69 -**

## 1. Introduction

### a. Three - Dimensional Television (3D TV)

As early as the 1920s, TV pioneers dreamed of developing high-definition three-dimensional (3D) color TV, as only this would provide the most natural viewing experience. During the next eighty years, the early black-and-white prototypes evolved into high-quality color TV, but the hurdle of 3D-TV still remains.

The term three-dimensional television (3DTV) is understood as a natural extension of two-dimensional television – which produces a flat image on a screen – into the third dimension. This means that the impression of the viewer also involves the perception of depth. Our two eyes view the world from slightly different positions and the two slightly different images registered by our eyes play a primary role in depth perception. The brain merges this information and creates the perception of a single 3D view. In the absence of the original scene or object, the same perception can be created by employing systems exploiting this mechanism.

The advent of three-dimensional television (3D TV) became of relevance in early 1990s with the introduction of the first digital TV services. The new type of media that expands the user experience beyond what is offered by now is being developed by the convergence of new technologies from computer graphics, computer vision, multimedia, and related fields.

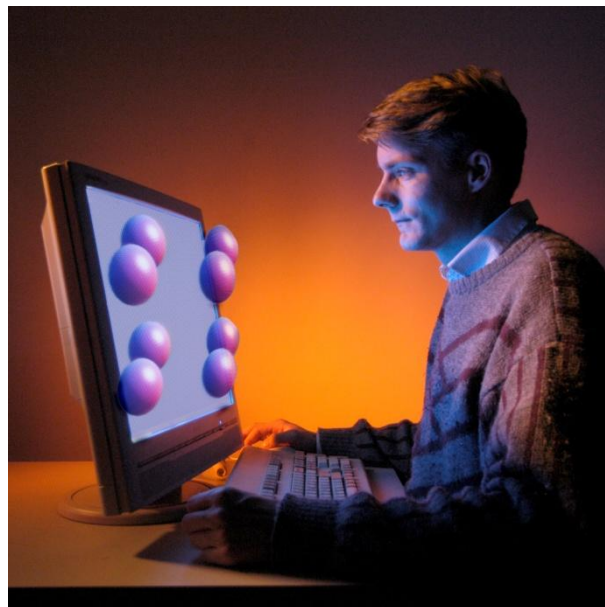


*Figure 1: Philips' lenticular lens 3-D display requires no special glasses and can show 3-D scenes simultaneously to several viewers. (Photo:Philips[1])*

## **b. Three-Dimensional Television; a chain of processes**

An integrated 3DTV system, involves different building blocks. The main blocks are: capturing of 3D moving scenes, their representation, rendering, compression and transport, and finally display.

In the entire processing chain there are numerous of challenges [2]. For the acquisition of dynamic scenes, an array of cameras is needed in most cases. The camera setups range from dense configuration (Stanford Light Field Camera, [3]) to intermediate camera spacing, [4], and wide camera distribution (Virtualized Reality<sup>TM</sup>, [5]).

For applications involving multiple cameras, camera calibration follows the acquisition of the scenes, in order to guarantee geometric consistency across the different cameras. The purpose of the calibration is to establish the relationship between 3D world coordinates and their corresponding 2D image coordinates. Once this relationship is established, 3D information can be inferred from 2D information and vice versa.

From the acquired multiview data, one should consider how to represent a 3D scene in a way that is suitable for latter processes: rendering, compression and transmission. Methods for 3D scene representation are often classified as a continuum between two extremes. The one extreme is represented by classical 3D computer graphics methods. This approach can be called geometry-based modeling, because the geometry of the scene is described in detail. The other extreme is called image-based modeling and does not use any 3D geometry at all. Purely image-based representations need many densely spaced cameras.

In the rendering stage, which is interrelated with the 3D representation, new views of scenes are reconstructed. Depending on the functionality required, there is a spectrum of renderings, from rendering with no geometry to rendering with explicit geometry. The technologies differ from each other in the amount of geometry information of the scene.

Having defined the data, efficient compression and coding is the next block in the 3D video processing chain. There are many different data compression techniques corresponding to different data representations, [6]. For example, there are different techniques for 3D meshed, depth data etc. The amount of multiview image data is usually huge, hence the data compressing and the data streaming are challenging tasks.

The display is the last, but definitely not least, significant aspect in the chain of 3D vision. The display is the most visible aspect of the 3DTV and is probably the one by which the general public will judge its success, [6]. Two main categories of 3D displays are available, those which imply personal specialized 3D headgear and those which do not (autostereoscopic displays) [7].

Displays in the first category, using personal headgear, are taking advantage of an obvious way to direct the views into the user's eyes. Examples are head mounted display systems and systems using LCD shutter glasses. Although these solutions can provide a great immersive 3D experience, the public reluctance to wear devices is discouraging their mass-market acceptance.

Autostereoscopic displays with tracking rely on real time tracking of the viewer position and projecting the left and right parts of a stereoscopic video stream into the corresponding user's eye. Current trackers and display optics are suited for a single-user 3D video experience only [8].

The ideal trackingless 3D displays shows so many images in different directions in space, that any viewer at any position sees different images with his left and right eye. Inherently, such a display serves multiple users, and provides them not only with stereo imagery but also with the motion parallax cue.

Current multi-view displays such as the Philips 3D-LCD [9] show in the order of 10 images, within a narrow zone, e.g.  $15^\circ$ , which is repeated over a wider viewing angle to serve multiple viewers.

### **c. Problem Statement**

To enable the use of 3DTV in real-world applications, the entire processing chain as discussed before needs to be considered. There are numerous challenges in this chain. In addition, there are strong interrelations between all the processes involved.

In this thesis the focus is set on the generation of the 3D content, and more specifically on the rendering part. The generation of 3D content is an active research area and lots of research works can be found in the current literature. First the state of the art methods are compared. Their advantages and disadvantages are discussed. The investigation of the methods shows that there is still space for improvement and that none of the current methods can completely accomplish the requirements of a 3DTV application.

We will introduce a new approach that matches better a 3DTV application. The approach is tested on real data and its feasibility to create 3D content is investigated. A couple of adaptations of the approach are also discussed.

This report has been structured as follows. The second chapter discusses related work. In this chapter the special requirements and the equipment available are also discussed and the research question is defined. The third chapter reviews the different analysis and rendering approaches that were used in the current project, discussing the steps from one approach to the other and the novelties that each of them introduces. In chapter four the experimental setup is described. The evaluation of the discussed approaches, objective and

subjective, is presented in chapter five. In chapter six the work conducted during this thesis project is discussed. Some open issues and ideas for future research are also stated.

## 2. Related work

Content availability is a factor that influences the success of 3DTV. Content production is a difficult task and it is even more difficult to create 3D effects in the content that are pleasing to the eye. As discussed before, a chain of interrelated stages have to be considered in order to enable the generation of 3D content. The Current literature with focus in the interrelated 3D representation and rendering stages is discussed in this chapter.

As said before, the methods for 3D scene representation and rendering are often classified as a continuum between two extremes. Geometry or model-based rendering and image-based rendering . In between the two extremes a number of methods exist which make use of both approaches and combine their characteristics.

### a. Model-based rendering (MBR) – rendering with explicit geometry

Geometry based rendering is used in applications such as games, Internet, TV and movies. The achievable performance with these models might be excellent, typically if the scenes are purely computer generated. The available technology for both production and rendering has been highly optimized over the last few years, especially in the case of common 3-D mesh representations. In addition, state-of-the-art PC graphic cards are able to render highly complex scenes with an impressive quality in terms of refresh rate, level of detail, spatial resolution, reproduction of motion, and accuracy of textures [2].

With the use of geometry-based representations quite sparse camera configurations are feasible, but most existing systems are restricted to foreground objects only [10,11,12] . In other words, despite the advances in 3-D reconstruction algorithms, reliable computation of full 3-D scene models remains difficult. In many situations, only a certain object in the scene– such as the human body- is of interest. Here, prior knowledge of the object model is used to improve the reconstruction quality.

Voxel-based representations, [13], can easily integrate information from multiple cameras but are limited in resolution. The work of Vedula et al., [13], based on the explicit recovery of 3D scene properties, first uses the so-called voxel coloring algorithm to recover a 3D voxel model of the scene at each time instant. The non-rigid motion of the scene between consecutive time instants is recovered, Figure 2. In the next stage, the voxel models and scene flow become inputs to a spatio-temporal view interpolation algorithm.

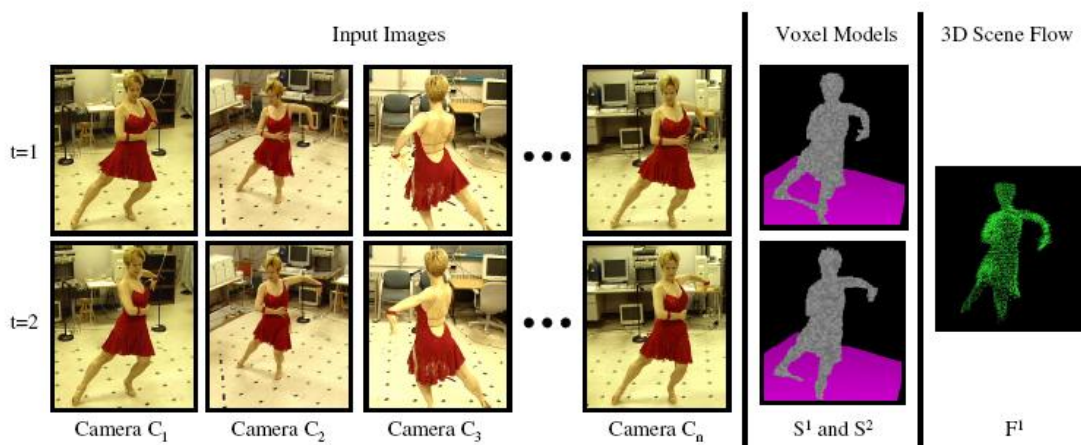


Figure 2: A set of calibrated images at 2 consecutive time instants. From these images, 3D voxel models are computed at each time instant using the voxel coloring algorithm. After computing the 3D voxel models, the dense non-rigid 3D motion or “scene flow” between these models is computed.

A prominent class of geometry reconstruction algorithms is shape-from-silhouette approaches. Shape-from-silhouette reconstructs models of a scene from multiple silhouette images or video streams. Starting from the silhouettes extracted from the camera pictures, a conservative shell enveloping the true geometry of the object is computed by reprojecting the silhouette cones into the 3-D scene and intersecting them. This generated shell is called the visual hull. While the visual hull algorithms are efficient and many systems allow for real-time reconstruction the geometry models they reconstruct are often not accurate enough for high-quality reconstruction of human actors.

Since scenes involving human actors are among the most difficult to reconstruct, research studies focused on free viewpoint videos of human actors can be found in literature. A typical example is the work of Carranza et al, [10], recently updated by Theobalt et al. [11], where a triangle mesh representation is employed because it offers a closed and detailed surface representation. Since the model must be able to perform the same complex motion as its real-world counterpart, it is composed of multiple rigid-body parts that are linked by a kinematic chain. The joints between segments are parameterized to reflect the object’s kinematic degrees of freedom. Besides object pose, the dimensions of the separate body parts also must be kept adaptable as to be able to match the model to the object’s individual stature.

A virtual reality modeling language (VRML) geometry model of a human body is used [Figure 3(a)]. Indicatively, the model consists of 16 rigid body segments, one each for the upper and lower torso, neck and head; and pairs of the upper arms, lower arms, hands, upper legs, lower legs, and feet. In total, more than 21,000 triangles make up the human body model.

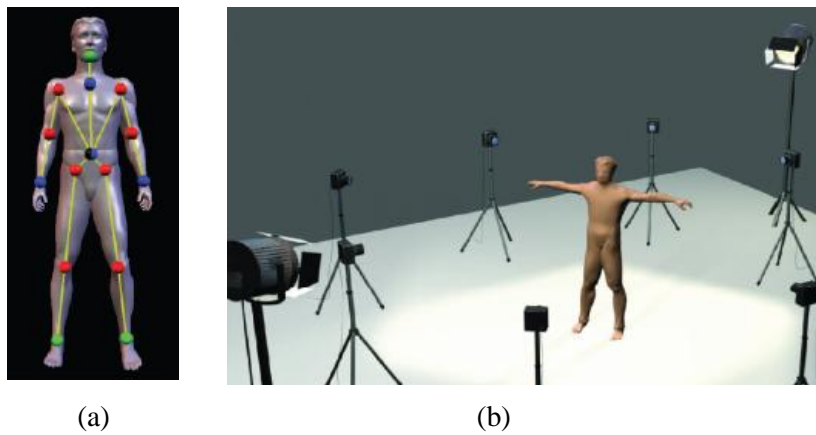


Figure 3: (a) Surface model and the underlying skeletal structure. Spheres indicate joints. (b) Typical camera and light arrangement during recording.

The challenge in applying model-based analysis for free-viewpoint video reconstruction is to find the way to adapt the geometry model automatically and robustly to the object's appearance as it was recorded by the video cameras. Since the geometry model is suitably parameterized to alter its shape and pose, the problem reduces to determining the parameter values that achieve the best match between the model and the video images. This task is regarded as an optimization problem.

The object's silhouettes, as seen from the different camera viewpoints, are used to match the model to the recorded video images. The foreground in all video images is segmented and binarized. At the same time, the 3-D object model is rendered from all camera viewpoints using conventional graphic hardware, after which the rendered images are thresholded to yield binary masks of the model's silhouettes. Then, the rendered model silhouettes are compared to the corresponding image silhouettes: as comparison measure, or matching score, the number of silhouette pixels is used that do not overlap when putting the rendered silhouette on top of the recorded silhouette. Conveniently, the logical exclusive-or (XOR) operation between the rendered image and the recorded image yields those silhouette pixels that are not overlapping. By summing over the non-overlapping pixels for all images, the matching score is obtained. To adapt model parameter values such that the matching score becomes minimal, a standard numerical nonlinear optimization algorithm runs on the CPU. For each new set of model parameter values, the optimization routine evokes the matching score evaluation routine on the graphics card. After convergence, object texture can be additionally exploited for pose refinement.

One advantage of model-based analysis is the low-dimensional parameter space when compared to general reconstruction methods (Figure 5): the parameterized 3-D model may provide only a few dozen degrees of freedom that need to be determined, which greatly reduces the number of potential local minima. Many high-level constraints are already implicitly incorporated into the model, such as kinematic capabilities. Additional constraints can be easily enforced by making sure that all parameter values stay within their anatomically plausible range during optimization.

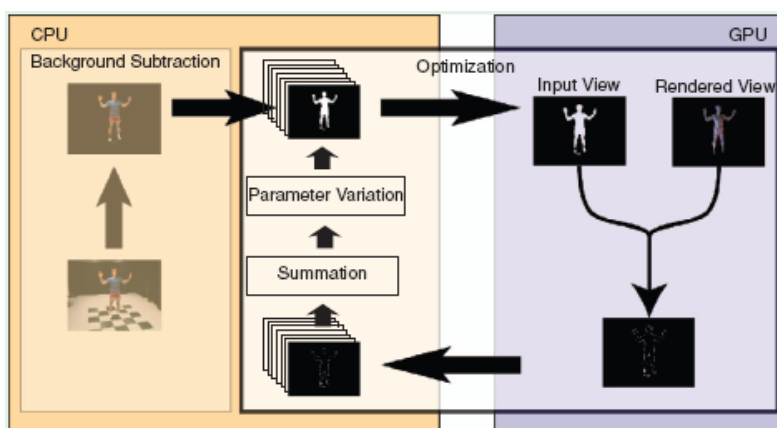


Figure 4: Analysis-by-synthesis: To match the geometry model to the multiview video footage, the foreground object is segmented and binarized, and the 3-D model is rendered from all camera viewpoints. The boolean XOR operation is executed between the reference images and the corresponding model renderings. The number of non-overlapping pixels serves as matching score. Via numerical optimization, model parameter values are varied until the matching score is minimal.



Figure 5: From eight video cameras spaced all around the scene, model-based method can capture the complex motion of a dancer.

After model-based motion capture, a high-quality 3-D geometry model is available that closely, but not exactly, matches the dynamic object in the scene. For photorealistic rendering results, the original video footage must be applied as texture to the model. Projective texture mapping is a well-known technique to apply images as texture to triangle-mesh models. To achieve optimal rendering quality, however, it is necessary to process the video textures offline prior to real-time rendering [10]: local visibility must be considered correctly to avoid any rendering artifacts due to the inevitable small differences between model geometry and the true 3-D object surface. Also, the video images, which are taken from different viewpoints, must be blended appropriately to achieve the impression of one consistent object surface texture.

Because model geometry is not exact, the reference image silhouettes do not correspond exactly to rendered model silhouettes. When projecting the reference images onto the model, texture belonging to some frontal body segment potentially leaks onto other segments farther back [Figure 6(a)]. To avoid such artifacts, each

reference view's penumbral region must be excluded during texturing. To determine the penumbral region of a camera, vertices of zero visibility are determined not only from the camera's actual position but also from a few slightly displaced virtual camera positions [Figure 6(b)]. For each reference view, each vertex is checked whether it is visible from all camera positions, actual as well as virtual. A triangle is projectively textured using a reference image only if all of its three vertices are completely visible from that camera.

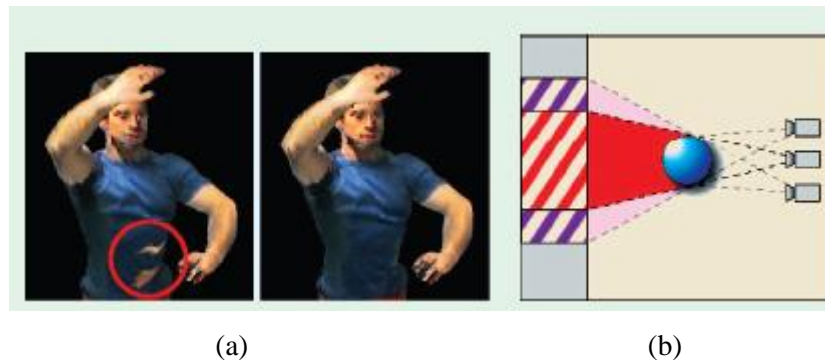


Figure 6: Penumbral region determination: (a) Small differences between object silhouette and model outline can cause texture of frontal model segments to leak onto segments farther back. (b) By projecting each reference image onto the model also from slightly displaced camera positions, regions of dubious visibility are determined. These are excluded from texturing by the respective reference image.

Most surface areas of the model are seen from more than one camera. If the model geometry corresponded exactly to that of the recorded object, all camera views could be weighted according to their proximity to the desired viewing direction and blended without loss of detail. However, model geometry has been adapted to the recorded person by optimizing only a comparatively small number of free parameters. The model is also composed of rigid body elements which is clearly an approximation whose validity varies, e.g., with the person's apparel. In summary, the available model surface can be expected to locally deviate from true object geometry. Accordingly, projectively texturing the model by simply blending multiple reference images causes blurred rendering results, and model texture varies discontinuously when the viewpoint is moving. Instead, by taking into account triangle orientation with respect to camera direction, high-quality rendering results can still be obtained for predominantly diffuse surfaces [10].

After uploading the 3-D model mesh and video cameras' projection matrices to the graphics card, the animated model is ready to be interactively rendered. During rendering, the multiview imagery, predetermined model pose parameter values, visibility information, and blending coefficients must be continuously uploaded, while the view-dependent texture weights are computed on the fly on the GPU.

## b. Image-based rendering (IBR) – rendering with no geometry

The other extreme in 3-D scene representation is called image-based rendering and does not use any 3-D geometry at all. The main advantage is a potentially high quality of virtual view synthesis avoiding any 3-D scene reconstruction. However, this benefit has to be paid by dense sampling of the real world with a sufficiently large number of natural camera view images. In general, the synthesis quality increases with the number of available views. Hence, typically a large number of cameras have to be set up to achieve high-performance rendering, and therefore a tremendous amount of image data needs to be processed. Contrarily, if the number of used cameras is too low, interpolation and occlusion artifacts will appear in the synthesized images, probably affecting the quality.

Examples of image-based representations are ray space or light field [14, 15] and panoramic configurations including concentric and cylindrical mosaics [16]. The underlying idea in most of these methods is capturing the complete flow of light in a region of the environment. Such a flow is described by a plenoptic function. The plenoptic function was introduced by Adelson and Bergen, [17], in order to describe the visual information available from any point space. It is characterized by seven dimensions, namely the viewing position  $(V_x, V_y, V_z)$ , the viewing direction  $(\theta, \varphi)$  or  $(x, y)$  in Cartesian coordinates, the time  $t$  and the wavelength  $\lambda$ . ( $I^{(7)}(V_x, V_y, V_z, \theta, \varphi, \lambda, t)$ ).

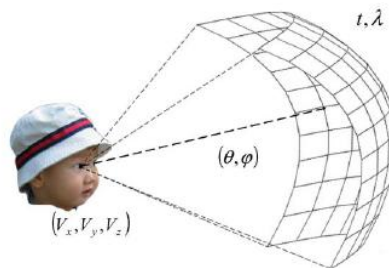


Figure 7: The 7D plenoptic function

The image-based representation stage is in fact a sampling stage, samples are taken from the plenoptic function for representation and storage. The problem with the 7D plenoptic function is that it is so general that due to the tremendous amount of data required, sampling the full function into one representation is not feasible. Research on image-based modeling is mostly about how to make reasonable assumptions to reduce the sample data size while keeping the rendering quality. One major strategy to reduce the data size is restraining the viewing space of the viewers. There is a common set of assumptions that people made for restraining the viewing space. Some of them are preferable, as they do not impact much on the viewers' experiences. Some others are more restrictive and used only when the storage size is a critical concern.

By ignoring wavelength and time dimensions, McMillan and Bishop [18] introduced plenoptic modeling, which is a 5D function:

$$I^{(5)}(V_x, V_y, V_z, \theta, \varphi)$$

They record a static scene by positioning cameras in the 3D viewing space, each on a tripod capable of continuous panning. At each position, a cylindrical projected image was composed from the captured images during the panning. This forms a 5D image-based representation: 3D for the camera position, 2D for the cylindrical image. To render a novel view from the 5D representation, the closely cylindrical projected images are warped to the viewing position based on their epipolar relationship and some visibility tests.

The most well-known image-based representations are the light field [15], and the Lumigraph [19] (4D). They both ignored the wavelength and time dimensions and assumed that radiance does not change along a line in free space. However parameterizing the space of oriented lines is still a tricky problem. The solutions they came out happened to be the same: light rays are recorded by their intersections with two planes. One of the planes is indexed with coordinate  $(u,v)$  and the other with coordinate  $(s,t)$ , i.e.:

$$l^{(4)}(s,t,u,v)$$

In Figure 8, an example where the two planes, namely the camera plane and the focal plane, are parallel is shown. This is the most widely used setup. An example light ray is shown and indexed as  $(u_0, v_0, s_0, t_0)$ . The two planes are then discretized so that a finite number of light rays are recorded. If all the discretized points from the focal plane are connected to one discretized point on the camera plane, we get an image (2D array of light rays). Therefore, the 4D representation is also a 2D image array, as is shown in Figure 9.

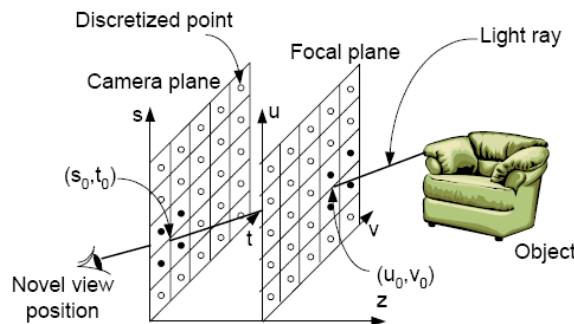


Figure 8: One parameterization of the light field.

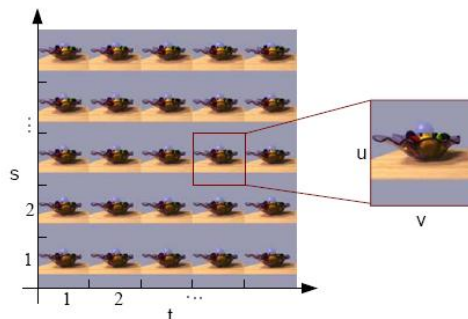


Figure 9: A sample light field image array: fruit plate.

The difference between light field and Lumigraph is that light field assumes no knowledge about the scene geometry. As a result the number of sample images required in light field for capturing a normal scene is

huge. On the other hand, Lumigraph reconstructs a rough geometry for the scene with an octree algorithm to facilitate the rendering (discussed later on) with a small amount of images. For this reason Lumigraph is sometimes classified as an hybrid and not a pure image-based modeling technique.

In the rendering stage in order to create a new view of the object, the view is splitted into its light rays, which are then calculated by quadlinearly interpolating existing nearby light rays in the image array. For example, the light ray  $(u_0, v_0, s_0, t_0)$  in Figure 8 is interpolated from the 16 light rays connecting the solid discrete points on the two planes. The new view is then generated by reassembling the split rays together. Such rendering can be done in real time and is independent of the scene complexity. Lumigraph, has also the advantage that can be constructed from a set of images taken from arbitrarily placed viewpoints. A re-binning process is therefore required. Geometric information is used to guide the choices of the basis functions. Because of the use of geometric information, sampling density can be reduced.

Other than the assumptions made in light field, concentric mosaics, [16], further restricts that both the cameras and the viewers are on a plane, which reduces the dimension of the plenoptic function to three. In concentric mosaics, the scene is captured by mounting a camera at the end of a level beam, and shooting images at regular intervals as the beam rotates, as is shown in Figure 10. The light rays are then indexed by the camera position or the beam rotation angle  $\alpha$ ; and the pixel locations  $(u, v)$ :

$$I^{(3)}(\alpha, u, v).$$

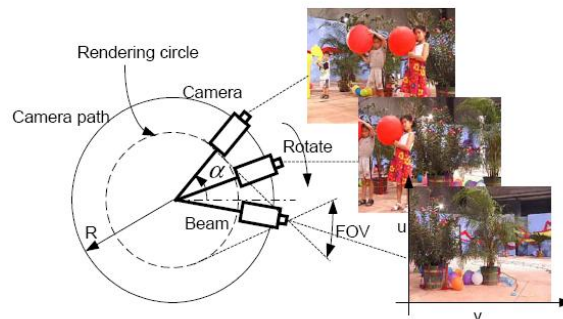


Figure 10: Concentric mosaic capturing

The rendering of concentric mosaics is slit-based. The novel view is split into vertical slits. For each slit, the neighboring slits in the captured images are located and used for interpolation. The rendered view is then reassembled using these interpolated slits. Although vertical distortions exist in the rendered images, they can be alleviated by depth correction. Concentric mosaics do not require the difficult modeling process of recovering geometric and photometric scene models. Yet they provide a much richer user experience by allowing the user to move freely in a circular region and observe significant parallax and lighting changes.

All these methods do not make any use of geometry, but they either have to cope with an enormous complexity in terms of data acquisition or they execute simplifications restricting the level of interactivity.

### c. Hybrid techniques – rendering with implicit geometry

In between the two above extremes, lies rendering with implicit geometry, a truly active research area. When 3D models of the objects and scene are unavailable, like in IBR techniques, user interaction is limited. If approximate geometry of objects in a scene can be recovered, then interactive editing of real scenes, which is one of the objectives of 3DTV, is facilitated.

A classical approach is the use of depth or disparity maps. Such maps assign a depth value to each sample of an image. Together with the original two-dimensional (2-D) image the depth map builds a 3-D-like representation, sometimes called 2.5-D, [20]. The point where implicit geometry becomes explicit is not very clear. In this report systems that use geometry information in the form of disparity maps are regarded as systems with implicit geometry, therefore rendering techniques using depth information are included in this chapter.

When the depth information is available for every point in one or more images, 3D warping techniques can be used to render nearby viewpoints. An image can be rendered from any nearby point of view by projecting the pixels of the original image to their proper 3D locations and re-projecting them onto the new picture. The most significant problem in 3D warping is how to deal with holes generated in the warped image. Holes are due to the difference of sampling resolution between the input and output images, and the disocclusion where part of the scene is seen by the output image but not by the input images. To fill in holes, the most commonly used method is to splat a pixel in the input image to several pixels in the output image.

Closer to the geometry-based end of the spectrum, methods are reported that use view-dependent geometry and/or view dependent texture [21]. Instead of explicit 3-D mesh models also point-based representations or 3-D video fragments can be used [22], (ETH).

Waschbusch et al, [22, 23], for example, proposes a view-independent point-based representation of the depth information. The ETH Institute, which is conducting this research, uses several so-called 3D video bricks that are capturing high-quality depth maps from their respective. Each brick is movable and contains one color, two grayscale cameras, and a projector. The matching algorithm used for depth extraction is assisted by the projectors illuminating the scene with binary structured light patterns. Texture and depth are acquired simultaneously.

Each brick acquires the scene geometry using depth from stereo algorithm. Depth maps are computed for the images of the left and right grayscale cameras by searching for corresponding pixels. Stereo matching is formulated as a maximization problem over an energy which defines a matching criterion of two pixel correlation windows. An adaptive correlation window is used covering multiple time steps only in the static part of the correlation windows. For the moving parts discontinuities in the image space are going to be

extended into the temporal domain, making correlation computation more difficult. Therefore the correlation window is extended in the temporal dimension, only for static parts, to cover three or more images.



Figure 11: The 3D video brick with cameras and projector (left), simultaneously acquiring textures (middle) and structured light patterns (right)

A two phase post processing is applied to the disparity images. First the regions of wrong disparity are identified and then new disparities are extrapolated into these regions from their neighbours.

To model the resulting three-dimensional scene, a view-independent, point-based data representation is used. All reconstructed views are merged into a common world reference frame. Three video bricks were used in the experiments of paper [23], thus three different views. The model is in principle capable of providing a full 360° view if the scene has been acquired from enough viewpoints. It consists of a set of samples, where each sample corresponds to a point on a surface and describes its properties such as location and color.

Every point is modeled by a three-dimensional Gaussian ellipsoid spanned by the vectors  $t_1, t_2, t_3$ , around its center  $p$ . This corresponds to a probabilistic model describing the positional uncertainty of each point by a trivariate normal distribution:

$$p_s(x) = N(x; p, V) = \frac{1}{\sqrt{(2\pi)^3 |V|}} e^{-\frac{1}{2}(x-p)^T V^{-1}(x-p)}$$

with expectation value  $p$  and covariance matrix

$$V = \Sigma^T \Sigma = (t_1 t_2 t_3)^T (t_1 t_2 t_3)$$

composed of 3 x 1 column vectors  $t_1$ .

Assuming a Gaussian model for each image pixel uncertainty, first the back-projection of the pixel into three-space is computed which is a 2D Gaussian parallel to the image plane spanned by two vectors  $t_u$  and  $t_v$ . Extrusion into the third domain by adding a vector  $t_z$  guarantees a full surface coverage under all possible views. This is illustrated in Figure 12.

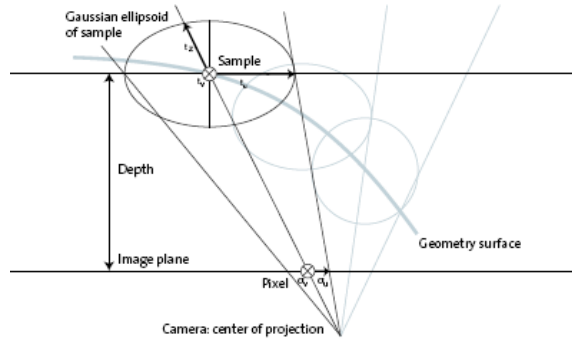


Figure 12: Construction of a 3D Gaussian ellipsoid.

Each pixel  $(u, v)$  is spanned by orthogonal vectors  $\sigma_u(1,0)^T$  and  $\sigma_v(0,1)^T$  in the image plane. Assuming a positional deviation  $\sigma_c$ , the pixel width and height under uncertainty are  $\sigma_u = \sigma_v = 1 + \sigma_c$ ,  $\sigma_c$  is estimated to be the average re-projection error of the calibration routine.

The depth of each pixel is inversely proportional to its disparity  $d$  as defined by the equation

$$z = - \frac{f_L |c_L - c_R|}{d + p_L - p_R}$$

Where  $f_L$  is the focal length of the rectified camera,  $c_L$  and  $c_R$  are the centers of projection, and  $p_L$  and  $p_R$ , the  $u$ -coordinates of the principal points. The depth uncertainty  $\sigma_z$  is obtained by differentiating the above equation and augmenting the gradient  $\Delta d$  of the disparity with its uncertainty  $\sigma_c$ :

$$\sigma_z = \frac{f_L |c_L - c_R|}{(d + p_L - p_R)^2} (\Delta d + \sigma_c)$$

After back-projection the point model still contains outliers and falsely projected samples. Some points originating from a specific view may look wrong from extrapolated views due to reconstruction errors, especially at depth discontinuities. In the 3D model, they may cover correct points reconstructed from other views, disturbing the overall appearance of the 3D video. Thus, those points are removed by checking the whole model for photo consistency with all texture cameras.

In the rendering stage they adopt an interesting approach described by Broadhurst et al., [24]. Broadhurst uses probabilistic volume ray casting to generate smooth images. Each ray is intersected with the Gaussians of the scene model. At a specific intersection point  $x$  with the sample  $i$ , the evaluation  $N(x;p_i;V_i)$  of the Gaussian describes the probability that a ray hits the corresponding surface point. To compute the final pixel color, two different approaches are described. The maximum likelihood method associates a color with the ray using only the sample which has the most probable intersection. The second approach employs the Bayes rule: it integrates all colors along each ray weighted by the probabilities without considering occlusions. Thus, the color of a ray  $R$  is computed as:

$$C_R = \frac{\int \sum_i c_i N(x; p_i, V_i)}{\int \sum_i N(x; p_i, V_i)}$$

The maximum likelihood method generates crisp images, but it also sharply renders noise in the geometry. The Bayesian approach produces very smooth images with less noise, but is incapable of handling occlusions and rendering solid surfaces in an opaque way. The rendering method that the authors propose combines both approaches in order to benefit from their respective advantages. The idea is to accumulate the colors along each ray like in the Bayesian setting, but to stop as soon as a maximum accumulated probability has been reached. Reasonably, a Gaussian sample should be completely opaque if the ray passes its center. The line integral through the center of a three-dimensional Gaussian has a value of  $1/2\pi$  and for any ray  $R$  it holds that:

$$\int_{x \in R} N(x; p, V) \leq \frac{1}{2\pi}$$

Thus, they accumulate the solution of the integrals of the above equation by traversing along the ray from the camera into the scene and stop as soon as the denominator of the equation reaches  $1/2\pi$ . Assuming that solid surfaces are densely sampled, the probabilities within the surface boundaries will be high enough so that the rays will stop within the front surface.

The results of comparison of this approach with the maximum likelihood and Bayesian rendering on noisy data are demonstrated in Figure 13. The large distortions in the maximum likelihood image, get smoothed out by the other two methods. However, the Bayesian renderer blends all the points including those from occluded surfaces, while current method renders opaque surfaces and maintains the blending.



Figure 13: Comparison of maximum likelihood (left) and Bayesian rendering (center) with Waschbusch et al.'s approach (right).

A representative result of the method is shown in Figure 14, where novel views of the acquired scene are rendered with the reconstructed 3D model. A sample video can be found in [25].



Figure 14: Re-renderings of the 3D video from novel viewpoints.

The model is in principle capable of providing a full  $360^{\circ}$  view if the scene has been acquired from enough viewpoints. Compared to mesh-based methods, points provide advantages in terms of scene complexity because they reduce the representation data and do not carry any topological information, which is often difficult to acquire and maintain. As each point in the model has its own assigned color, they also do not have to deal with texturing issues. Moreover, a view-independent representation is very suitable for 3D video editing applications since tasks like object selection can be achieved easily with standard point processing methods.

The point based data representation model is in general suitable for 3DTV applications but still contains many redundancies. Big clusters of outliers tend to grow in the discontinuity optimization stage if they dominate the correct depths in a color segment. Furthermore as the authors acclaim the resulting image quality could also be improved by exploiting inter-brick correlation and eliminating remaining artifacts at silhouettes using matting approaches as done by Zitnick et al. [4].

Zitnick et al., [4], propose a quite sophisticated representation. First, guided by the fact that using a 3D impostor or proxy for the scene geometry can greatly improve the quality of the interpolated views, they generate and add per-pixel depth maps (multiple depth maps for multiple views). However, even multiple depth maps still exhibit artifacts (at the rendering stage) when generating novel views. This is mainly because of the erroneous assumption at the stereo computation stage, that each pixel has a unique disparity. This is not the case for pixels along the boundary of objects that receive contributions from both the foreground and background colors.

Zitnick addresses this problem using a novel two-layer representation inspired by Layered Depth Images [26]. The two layer representation is one of the most efficient rendering methods for 3D objects with complex geometries and it was proposed already in 1998 by Shade et al.

A Layered Depth Image is an array of layered depth pixels ordered from closest to furthest from a so-called LDI camera. Each layered depth pixel contains multiple depth pixels at per-pixel location. The farther depth pixels, which are occluded from the viewpoint at the center of LDI camera, will appear as the viewpoint

moves away from the center of LDI camera. This image-based rendering technique is an abstract of depth images, which assigns a z-value in addition to the x and y values normally associated with a pixel.

When rendering from an LDI, the requested view can move away from the original LDI view and expose surfaces that were not visible in the first layer. The previously occluded regions may still be rendered from data stored in some later layer of a layered depth pixel.

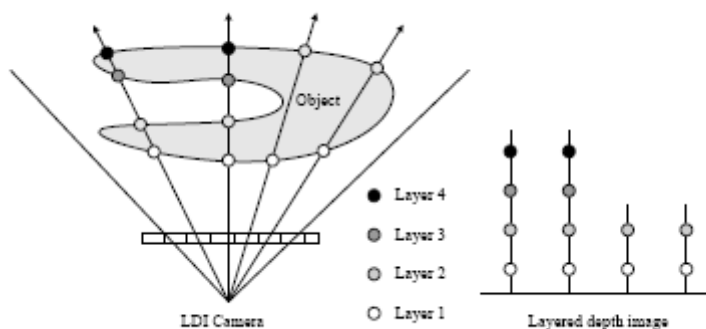


Figure 15: Layered Depth Image (LDI) and LDI camera

There are two ways to generate an LDI from natural images: generate LDI from multiple depth images and generate LDI from real images directly [26], illustrated as in Figure 15. If multiple color and depth images from natural images are obtained, the LDI is constructed by warping pixels in other camera locations, such as C1 and C2. Otherwise, The LDI can be generated directly from the input images by an adaptation of Seitz and Dyers voxel coloring algorithm [27]. The voxel coloring method assigns colors to voxels (points) in a 3D volume so as to achieve consistency with a set of basis images. In [27], a ordinal visibility constraint is exploited in order to simplify visibility relationships. In particular, it becomes possible to partition the scene into a series of voxel layers that obey a monotonic visibility relationship: for every input image, voxels only occlude other voxels that are in subsequent layers. Consequently, visibility relationships are resolved by evaluating voxels one layer at a time.

The voxel coloring algorithm visits each of the  $N^3$  voxels exactly once and projects it into every image. Therefore, the time complexity of voxel coloring is  $O(N^3n)$ , where  $n$  the number of images. Such a complexity prohibits the use of the algorithm for the modeling of a whole scene.

Zitnick, [4], overcomes this constraint, by calculating the matting, or second layer information, in specific areas and not for the whole scene. Matting information is computed within a neighbourhood of four pixels from all depth discontinuities. A depth discontinuity is defined as any disparity jump greater than  $\lambda$  ( $\lambda=4$ ) pixels. Within these neighborhoods, foreground and background colors along with opacities (alpha values) are computed using Bayesian matting [28]. The foreground information is combined to form the boundary layer as shown in Figure 16. The main layer consists of the background information along with the rest of the

image information located away from the depth discontinuities. Chuang et al.'s algorithm do not estimate depths, only colors and opacities. Depths are estimated by using alpha-weighted averages of nearby depths in the boundary and main layers. To prevent cracks from appearing during rendering, the boundary matte is dilated by one pixel toward the inside of the boundary region.

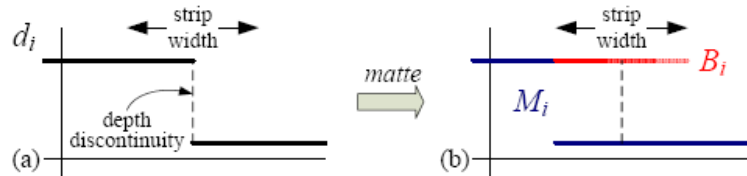


Figure 16: Two-layer representation: (a) discontinuities in the depth are found and a boundary strip is created around these; (b) a matting algorithm is used to pull the boundary and main layers  $B_i$  and  $M_i$  (The boundary layer is drawn with variable transparency to suggest partial opacity values)

Figure 17 shows the results of applying the stereo reconstruction and two-layer matting process to a complete image frame. It is noticeable that only a small amount of information needs to be transmitted to account for the soft object boundaries, and how the boundary opacities and boundary/main layer colors are cleanly recovered.

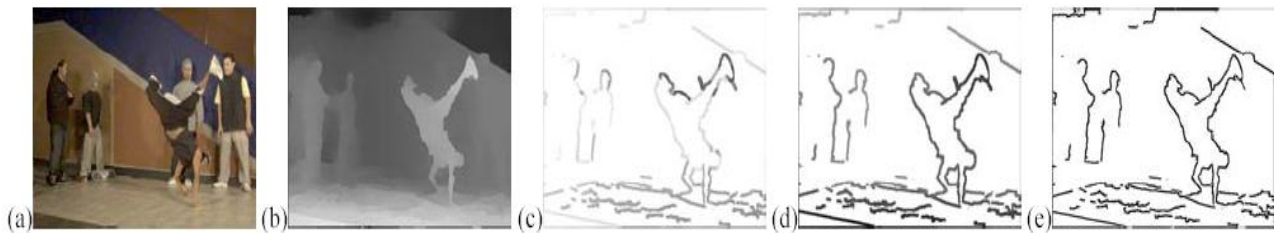


Figure 17: Sample results from matting stage: (a) main color estimates; (b) main depth estimates; (c) boundary color estimates; (d) boundary depth estimates; (e) boundary alpha (opacity) estimates. For ease of printing the boundary images are negated, so that transparent empty pixels show up as white.

In the rendering stage, given a novel view, the nearest two cameras in the data set are picked. For each camera the main data and boundary data are projected into the virtual view. The results are stored in separate buffers each containing color, opacity and depth. These are then blended to generate the final frame.

The layered depth image approach, provides results with quite good visual quality. However, even for an approach like Zitnick's dense scene sampling is necessary. For example in order to achieve coverage about  $30^\circ$ , a configuration of 8 cameras was used. The discussed approach processes each camera independently from the others. Better quality could be obtained by merging data from adjacent views when trying to estimate the semi-occluded background. This would also allow the multi-image matting to get even better estimates of foreground and background color and opacities.

#### **d. Compatibility with 3DTV applications**

This thesis addresses several problems and constraints discussed here. Motivation to test a new approach emanates from the special requirements that a 3DTV application has. The fact that the 3D video should include not only the foreground objects but also the background is considered as a premise.

The flexibility and scalability, important characteristics of an efficient approach, motivate the use of a per-pixel algorithm. Per-pixel operations allow flexibility in the sense that their complexity depends on the resolution of the initial images. Therefore, computational cost could be decreased by using low quality images, or increased when high resolution initial images are used. The scalability is important, in the sense that more cameras can be added, and in this case the algorithm preserves its characteristics but the quality of the final result is refined, or a wider view range is feasible. Parallel computation, that is feasible for independent per-pixel operations, could also facilitate a real time system.

The approaches discussed in chapter three are also motivated from the limited recording facilities (low number of cameras) available in the studio at the university. An approach that would be able to generate a 3D video captured initially by four stereo cameras, of 640x480 resolution, was a challenging task considering the current literature studies demanding dense camera configurations. Motivated from 3DTV requirements and state of the art limitations is therefore the work presented in the next chapters of this thesis project.

### 3. Rendering

The 3D video acquisition system used in this thesis consists of four calibrated pairs of stereo cameras that are capturing high quality images (640x480) from their respective viewpoints. Therefore the input, of the algorithms discussed in this chapter, is eight images from different viewpoints, as shown in the following Figure.

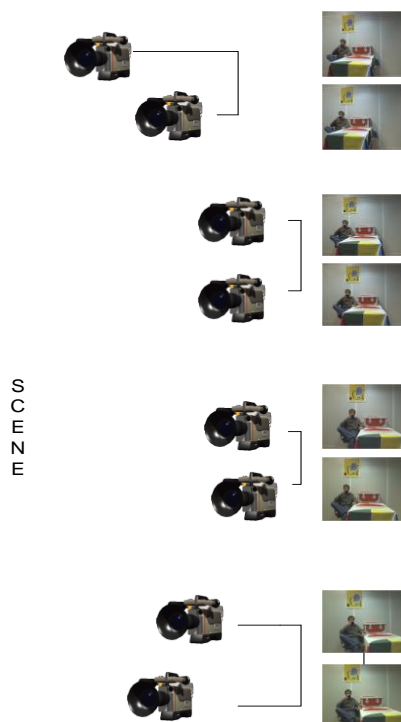


Figure 18: Four stereo cameras are used, capturing in total 8 images.

Starting point of the investigation of an algorithm that would fulfill the 3DTV requirements was a standard used in the ICT group. This approach does not follow the typical order of stages, as this was discussed in chapter one. The 3D representation and rendering stage are substituted by an analysis stage, analyzing the information from all the eight cameras, and a rendering stage, in which the virtual views are being generated. Virtual are considered the views from positions (virtual camera positions) where cameras were not originally placed (Figure 19).

The two stages, 3D representation and rendering, are strongly interrelated. There is no intermediate representation, which means that every time a new virtual view has to be generated the analysis stage has to run before.

The method is using per-pixel operations. Characteristics and features, that neighboring pixels may have in common, are not taken into account. This has the advantage that gives the method freedom, to regenerate only part of one view for example without loss of accuracy. The drawback is of course that it does not

consider properties of neighboring pixels that could be useful and save computational load in an object-based approach for example.

### a. Basic approach

In order to generate a new view, at a virtual position a ray tracing scheme is adopted. Every pixel of the virtual view is considered independently. Figure 19 is illustrating the method with a one pixel example. This pixel comes from a depth position in the 3D scene. In order to figure out its depth position different depth values are tested.

This is conducted as follows: a light ray is constructed for the pixel under consideration. The ray is modeling all possible depths of the pixel. Therefore it should be able to model all the depth positions possible in the original 3D scene. A step for the depth is selected. For the whole range of depths, one depth-step at a time from the virtual view's pixel is projected to all the original images. The pixels on which is projected are the corresponding pixels for the given depth.

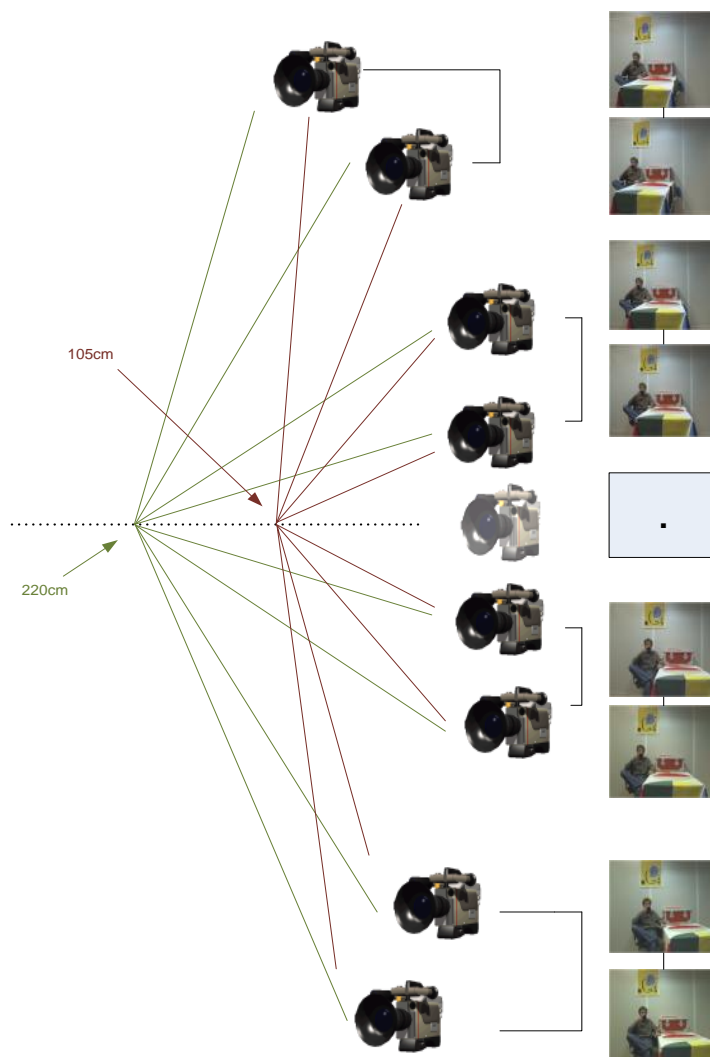


Figure 19: Here two different depth hypotheses (105cm, 220cm) are projected to the original images.

The pixel in every original image matching the given depth should have an RGB value. In case the projection of a depth does not correspond to a pixel within the borders of the original image then this original image is not considered effective and is not participating in the regeneration of the virtual view.

By collecting the RGB values, a set of  $N_{\text{cams}} \times 3$  values is formed, where  $N_{\text{cams}}$  the number of effective cameras. The mean value,  $\mu$ , and the variance,  $\sigma^2$ , of the color in this dataset are computed for each of the three color components:

$$\mu_k(z) = \frac{\sum_{c=1}^{N_{\text{cam}}} k_c(z)}{N_{\text{cam}}(z)} \quad (1)$$

$$\sigma_k^2(z) = \frac{\sum_{c=1}^{N_{\text{cam}}} k_c^2(z)}{N_{\text{cam}}(z)} - \mu_k^2(z) \quad (2)$$

where  $k = r, g, b$ , and r stands for the red color component, g for the green and b for the blue.  $N_{\text{cam}}$  stands for the number of effective cameras, and c is the index of the cameras. The r, g, b color variances are then summed up:

$$\sigma_{RGB}^2(z) = \sigma_r^2(z) + \sigma_g^2(z) + \sigma_b^2(z) \quad (3)$$

The RGB color variance as it appears in equation 3 is calculated for every step of the ray, or in other words for every depth hypothesis. In case the depth hypothesis is correct the variance should have a low value. This happens because for the correct depth, the original cameras should be in agreement, since they should be viewing the same scene point, and the collected RGB values should converge. A high variance implies disagreement among the cameras, and is not in general the case of a correct depth.

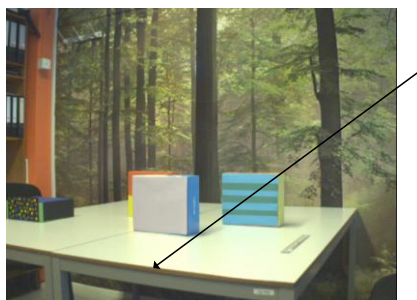
Therefore from all the depth hypotheses, the one with the lowest variance is selected.

$$z_{\text{SEL}} = \min_z \sigma_{RGB}^2(z) \quad (4)$$

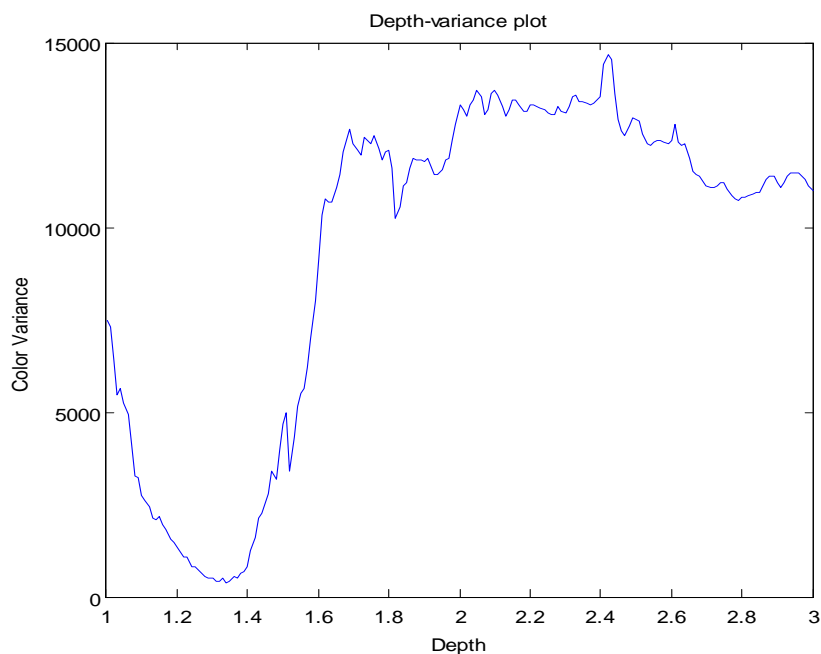
For this depth the mean RGB value of all the effective cameras is assigned to the new pixel.

The computed variance for one pixel in a virtual view as a function of possible depths is plotted in Figure 20.

The pixel under consideration is a pixel at the front part of the scene, on the table.



(a)



(b)

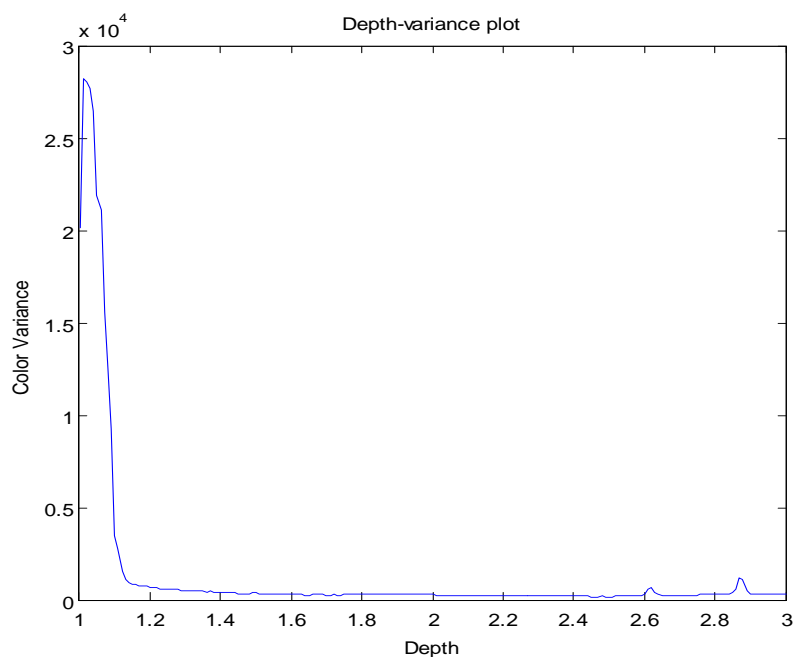
Figure 20: (a): The depth hypothesis for a pixel at the front part of the table is visualized. (b): Depth-variance diagram. The above diagram is a visualization of the variance of the pixel indicated in (a) for all the depths from 1m to 3m.

In this diagram there is a clear mode (minimum), at 1.35 meters and this is the depth that will be selected. However there are cases where the depth-variance diagram has not a clear minimum value. Possible causes of such cases are e.g. homogeneous areas or cases of occlusion.

An example of a homogeneous area is the white table, illustrated with an arrow in the next figure. The table is not covering only one specific depth in the scene. The depth – variance diagram is shown as well and it is obvious that in this case, the original cameras are in an agreement, for a wide range of depths.



(a)



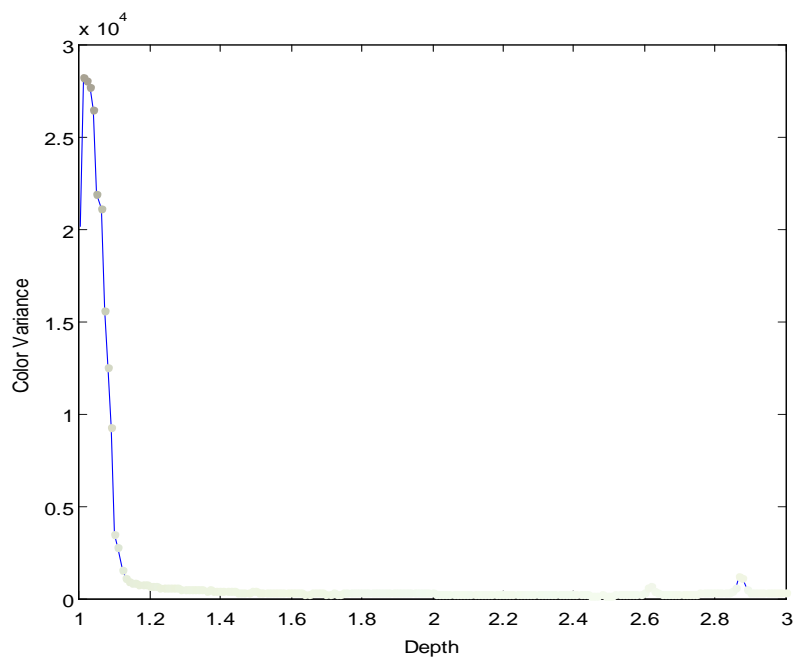
(b)

Figure 21: (a): The depth hypothesis for a pixel on the white table is visualized. (b): Depth-variance diagram. The above diagram is a visualization of the variance of the pixel indicated in (a) for all the depths from 1m to 3m.

The depth that is going to be selected by the algorithm may not be the correct one. It would be the one with the lowest variance, but in this case this is not a safe criterion. In Figure 22, the mean RGB values, as they were calculated for every depth are also plotted. For depth from 1.2 meters to 3 meters the color is white, with some small changes probably due to illumination changes. Although the selected depth could be wrong, the color of the pixel in the regenerated view is going to be correct.



(a)



(b)

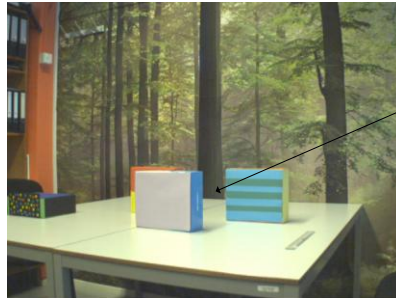
Figure 22: (a): The depth hypothesis for a pixel on the white table is visualized. (b) Depth-variance diagram for the pixel indicated in for all the depths from 1m to 3m. (a). The dots scattered in the diagram indicate the mean RGB value for each depth.

Therefore homogeneous areas may be responsible for errors in the depth map of the scene but are not causing any artifacts in the final image.

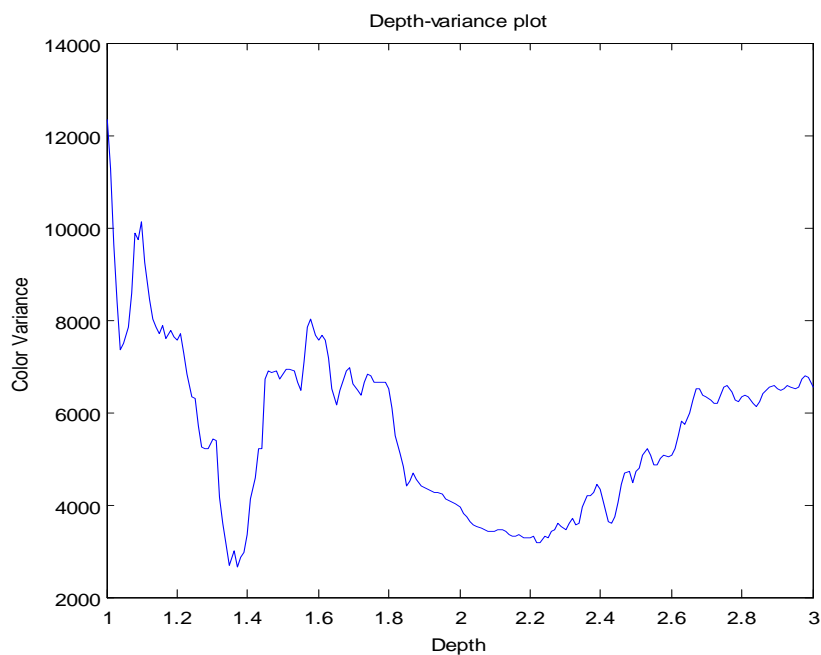
The occlusion problem occurs when part of the objects which constitute the scene, or part of the background is covered by other objects. In this application where multiple cameras are used, occluded areas can be present at some of the images captured by the original cameras or even in all of them. This causes spread within the set of the collected RGB values.

A pixel between the two boxes at the right is selected and its depth-variance results are visualized. The original cameras seem not to agree for the RGB values corresponding to pixels in this area. The cause of the disagreement is that for some of the 8 original cameras the purple box is occluding the background, for some

of them the stripped box is occluding the background and there are also those cameras which are capturing the background. The depth hypothesis is therefore not valid, since the correct depth may be not the one with the lowest variance.



(a)



(b)

Figure 23: (a): The depth hypothesis for a pixel at the background is visualized. (b): Depth-variance diagram. The above diagram is a visualization of the variance of the pixel indicated in (a) for all the depths from 1m to 3m.

## b. Weighted approach

In order to overcome the problem of occlusion, and make the discussed approach compatible with the regeneration of occluded areas, the proximity of the original cameras to the virtual view is considered.

In current literature camera proximity has been widely used. In the work of Min et al. for example [29], given a viewpoint the nearest two images (camera  $i$  and  $i+1$ ) are selected and projected into virtual view. Smolic et al. as well in [30], using a multicamera setup, are building 3D video objects. In order to project the textures from the original views onto the geometry, voxel models, they are calculating a weight. For each projected texture a normal vector  $n_i$  is defined pointing into the direction of the original camera. For

generation of a virtual view into a certain direction  $v_{VIEW}$  a weight is calculated for each texture, which depends on the angle between  $v_{VIEW}$  and  $n_i$ .

The weighted interpolation ensures that at original camera positions the virtual view is exactly the original view. The closer the virtual viewpoint is to an original camera position the greater the influence of the corresponding texture on the virtual view.

The approach discussed at the beginning of this chapter is therefore adapted in order to integrate the original camera – virtual view position proximity. Every time a virtual view at a new position is calculated, a weight is assigned to every original camera:

$$w_c = \frac{1}{((x_c - x_{vv})^2 + (y_c - y_{vv})^2 + (z_c - z_{vv})^2 + 10^{-4})} \quad (5)$$

Where  $(x_{vv}, y_{vv}, z_{vv})$  is the position of the virtual view, and  $(x_c, y_c, z_c)$  the position of the original camera  $c$ . The weight is different for every, of the  $c = [1, 8]$ , original cameras. When the distance approaches zero, the weight gets a great value, but it can never approach infinity, due to the  $10^{-4}$  factor. We assumed that the minimum distance between a camera and a virtual view is  $1\text{cm} = 10^{-2}$ . So, the squared minimum distance gives the factor  $10^{-4}$ . In case the projection to one of the cameras is not effective, it is projected out of borders as already discussed this camera is assigned a zero weight.

The weights of the cameras are participating in the calculation of color variance. The color variance is now calculated as follows:

$$\mu_{WEIGHT, k}(z) = \frac{\sum_{c=1}^8 w_c k_c(z)}{\sum_{c=1}^8 w_c} \quad (6)$$

$$\sigma_{WEIGHT, k}^2(z) = \frac{\sum_{c=1}^8 w_c k_c^2(z)}{\sum_{c=1}^8 w_c} - \mu_{WEIGHT, k}^2 \quad (7)$$

where  $k = r, g, b$ .

The  $r, g, b$  weighted color variances are then summed up:

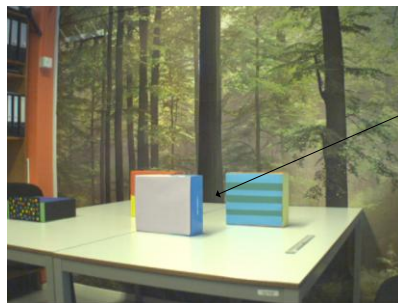
$$\sigma_{WEIGHT, RGB}^2(z) = \sigma_{w,r}^2(z) + \sigma_{w,g}^2(z) + \sigma_{w,b}^2(z) \quad (8)$$

The weighted color variance is calculated for every depth hypothesis. The depth with the lowest variance is selected:

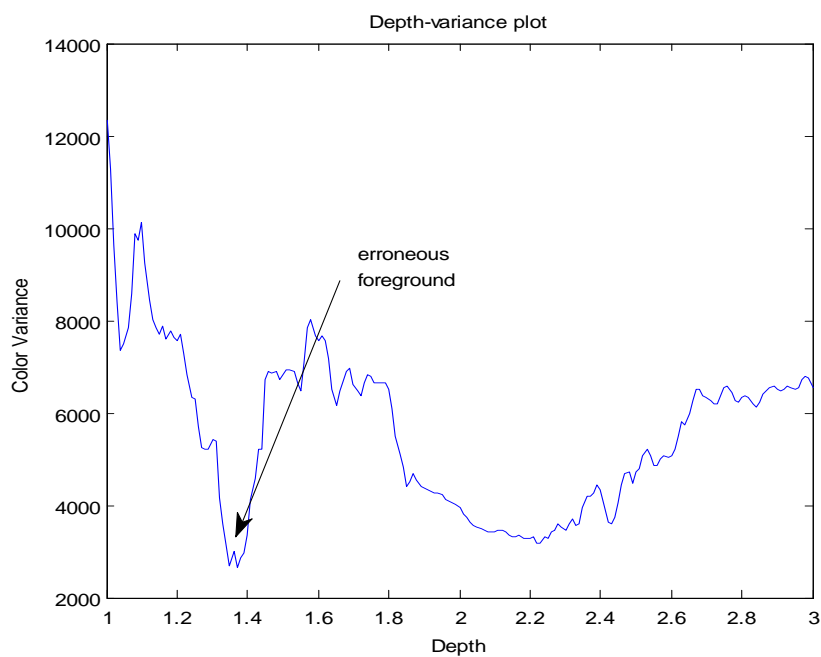
$$z_{WEIGHT\_SEL} = \min_z \sigma_{WEIGHT\_RGB}^2(z) \quad (9)$$

and its the mean RGB value as calculated in (6) is assigned to the pixel.

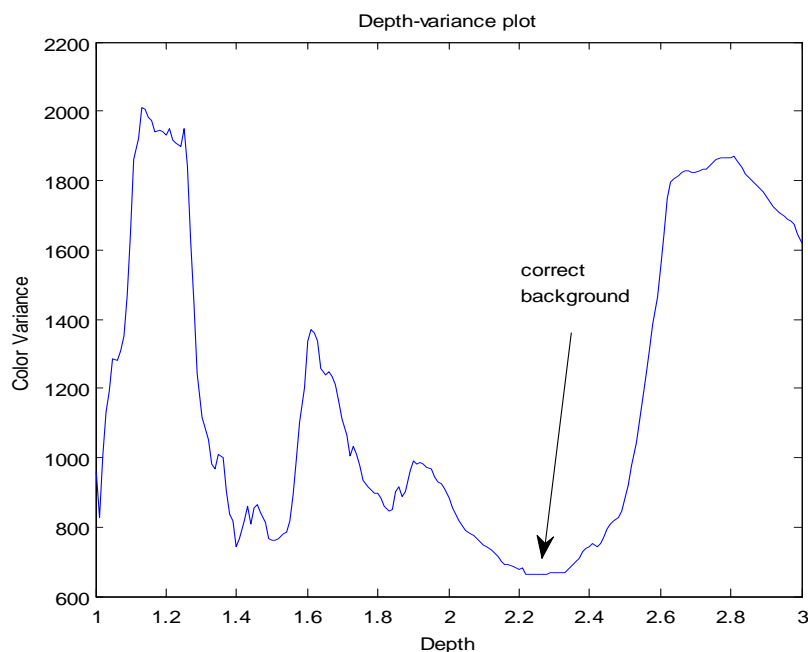
The depth-variance diagram, influenced from the camera proximity is shown in the next figure, for a pixel in the area with occlusion, between the two boxes.



(a)



(b)



(c)

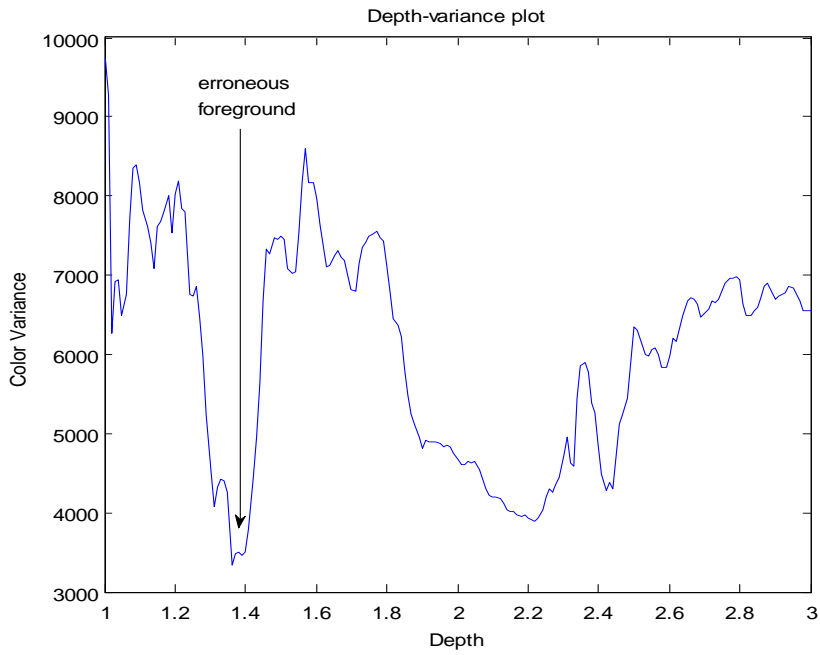
Figure 24: (a): The depth hypothesis for a pixel at the background is visualized. (b,c): Depth-variance diagrams. The diagrams are visualizations of the variance of the pixel for all the depths from 1m to 3m. (b) non-weighted variance, (c) weighted variance.

In Figure 24, the depth variance diagram for the first approach discussed in chapter 3.a and the weighted variance diagram are illustrated. The pixel under consideration is between the two boxes and it belongs to the background. When the first approach is used (Figure 24.b), the lowest variance is around 1.4 meters. This depth corresponds to the box and is erroneously selected. In the weighted approach the cameras at positions close to the virtual view have a stronger impact on the variance. The lowest variance is now detected for depths around 2.2 meters (depth that corresponds to the background).

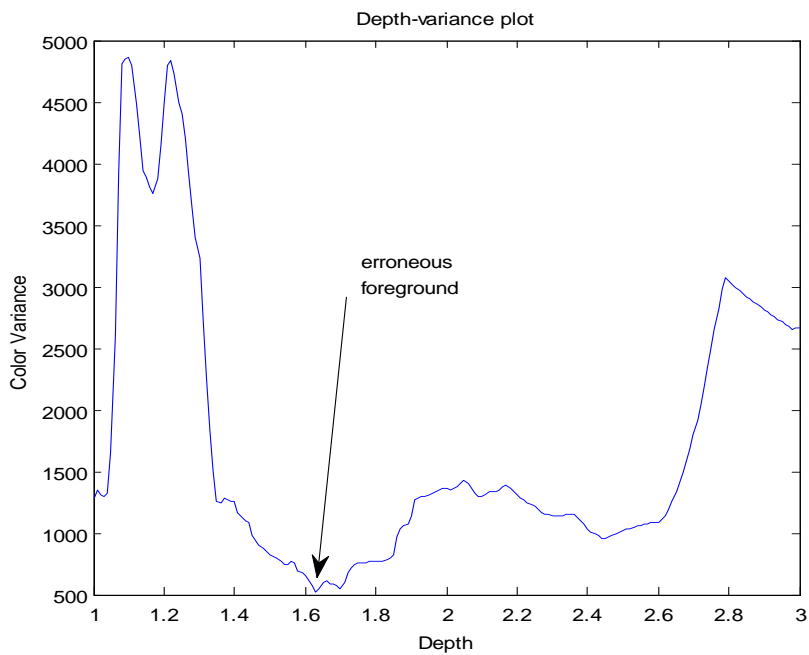
### c. Outlier removal approach

The weighted approach could solve the occlusion problem but only partially. There are still artifacts appearing in the regenerated images. In case of occlusion, or in case of illumination changes for example, it can happen that the cameras are viewing different colors even for the correct depth. An insight on the values of the cameras for pixels with erroneous colors, shows that the main cause of the errors is the existence of outlier values.

Taking as an example a second pixel, neighboring to the one appearing in Figure 24, thus within the occluded area, it turns out that for this pixel the weighted approach is not working.



(a)



(b)

Figure 25: Depth-variance diagrams of a pixel in the occluded area. The diagrams are visualizations of the variance of the pixel for all the depths from 1m to 3m. (a) non-weighted variance, (b) weighted variance.

Although the weights influence the variance of the cameras, the depth with the lowest  $v$  is erroneously around 1.6 meters (the ground truth lies around 2.2 meters). A plot of the RGB values of the eight cameras indicates the cause of the error:

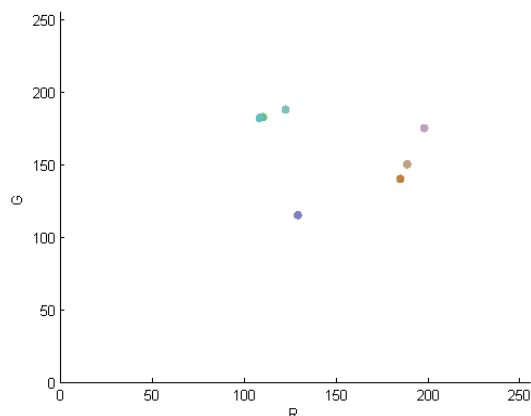


Figure 26: The dots in the diagram stand for the colors of the eight cameras, for depth 2.2 meters. The color of the dot represents the RGB color of the camera. The dots are plotted in the RG space.

For the correct depth four of the cameras are viewing the stripped box, one of them the purple box and the rest three cameras the background. The variance is calculated for all the cameras, therefore if outliers are present for the correct depth, this is not going to be selected by the algorithm. Probably there will be another depth value for which the camera values would be less spread.

Solution to this cause of errors is the removal of the outlier values. There are plenty of methods for the removal of the outliers. A binary classification of the input data into inlier and outlier class could be achieved with RANSAC, [31], or major vote method. Hard clustering, assigns each data point (feature vector) inside with a degree of membership equal to one or outside the cluster, with a degree of membership zero.

In our application the borderline between inliers and outliers is not crisp. There is much controversy on what constitutes an outlier. The borderline depends on the specific scene, and could have a strong effect on the sharpness of the final image.

In order to have the flexibility to handle such situations, by adapting the parameters of the algorithm for example, a non –binary clustering algorithm without a priori assumptions on the number of clusters is used.

The method used resembles the mean shift algorithm, an algorithm used broadly in image processing applications, for image segmentation for example, [32], (Appendix D). The mean shift and the algorithm used here as well are unsupervised. The clusters and the outliers are identified using an iterative scheme.

The location of the cluster centroids is not known a priori. Here, the mean value of the RGB values as calculated in (4), (the weights of the cameras are not used here), is the starting vector  $O^t$ . The index  $t$  stands for the number of iterations ( $t > 0$ ).

The RGB values of each of the eight cameras, are represented by a vector  $V_c$ , ( $c \in [1,8]$  stands for the number of the camera).  $V_c$  is therefore a  $3 \times 1$  vector, containing information for the three color components of camera  $c$ . The eight  $V_c$  vectors constitute the dataset of the algorithm.

The distance,  $d_c^t$ , of the initial mean value  $O^t$ , with respect to each vector  $V_c$  is calculated as:

$$d_c^t(z) = \left| O^t(z) - V_c(z) \right|^2 \quad (10)$$

and is an estimate of the variance of the  $V_c$  values.

The cameras for which the distance is high are considered outliers, whereas those with low distance value are considered inliers. Therefore a scalar weight is assigned to each of them, computed as the inverse of the sum of the distances plus a  $\delta$  indicating the minimum acceptable size of a cluster:

$$w_{OUTR_c}^t(z) = \frac{1}{d_c^t(z) + \delta} \quad (11)$$

The weights of the cameras are normalized, and a new vector for the next iteration is defined as:

$$O^{t+1}(z) = \sum_{c=1}^8 w_{OUTR_c}^t(z) V_c(z) \quad (12) \quad , \quad \text{with} \quad \sum_{c=1}^8 w_{OUTR_c}^t(z) = 1 \quad (13)$$

The distance of the starting value  $O$  from the vectors  $V_c$  is calculated again, new weights are assigned to the cameras and the starting value  $O$  is recomputed with the new camera weights.

The iterative procedure stops when a predefined number of iterations are executed. The sequence of points should finally converge to one of the so-called attractors of the iterative scheme. This is the final centroid of the cluster.

With the method described above, none of the cameras has a zero weight. Even the cameras that are considered outliers are assigned a very small weight which may practically exclude them from the calculation of centroid of the cluster (the final RGB mean value).

At the end of the iterative process a number indicating the number of the cameras that are practically participating in the calculation of the mean value (effective number of member-cameras) is computed.

$$N(z) = e^{-\sum_{c=1}^8 w_{OUTR_c}^t(z) \log w_{OUTR_c}^t(z)} \quad (14)$$

where  $w_{OUTR_c}^t = w_{OUTR_c}^\infty$ , the weights after the iterations.

There are different ways to integrate the outlier removal method in the sequence of processes. One possible scenario, is first to select the depth, using the approach discussed at chapter 3.a, based on the color variance (the camera proximity weights may be used as well). Then for the selected depth, which probably contains outlier values, the outlier removal method can be performed. The mean value RGB value, the value that would be finally assigned to the pixel, would be recalculated without the outliers.

This approach saves computational cost, since the outlier removal method which is quite expensive is executed only once for every pixel. However, is non-optimal. The initial RGB values and the color variances calculated for all the depths include outliers. A less compromising scenario, in terms of accuracy and correctness of the final result, is to use the outlier removal method for all the possible depths before the calculation of the variance.

Therefore what we investigated is first to remove the outliers from the set of the RGB values of the original cameras and then proceed with the selection of the depth.

In more detail, given a pixel and a depth, the outlier removal method outputs weights for all the cameras,  $w'_{OUTR_c}$ . These weights can be used to calculate the new mean and variance (non-weighted outlier removal approach). Only removing the outliers was tested and did not give sufficient results therefore the outlier removal weights have been linearly combined with the camera proximity weights,  $w_c$  (weighted outlier removal), as calculated in (6):

$$w_{FINAL_c}(z) = w'_{OUTR_c}(z) + 0.7w_c \quad (15)$$

The 0.7 factor was assigned to the camera proximity weights based on experimental observations and the fact that their influence should not overcome the outlier removal weights.

The mean RGB value is recalculated based on the new combined weights of the cameras. The variance of the eight RGB values from the center of the cluster (the new mean value) also.

$$\mu_{FINAL,k}(z) = \frac{\sum_{c=1}^8 w_{FINAL_c} k_c(z)}{\sum_{c=1}^8 w_{FINAL_c}} \quad (16)$$

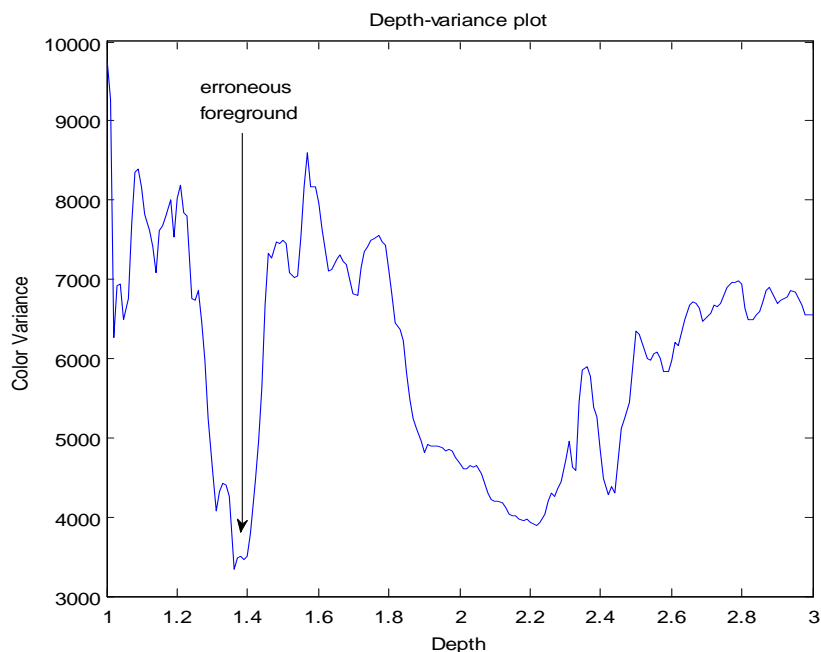
$$\sigma_{FINAL,k}^2(z) = \frac{\sum_{c=1}^8 w_{FINAL_c} k_c^2(z)}{\sum_{c=1}^8 w_{FINAL_c}} - \mu_{FINAL,k}^2 \quad (17)$$

where  $k = r, g, b$ .

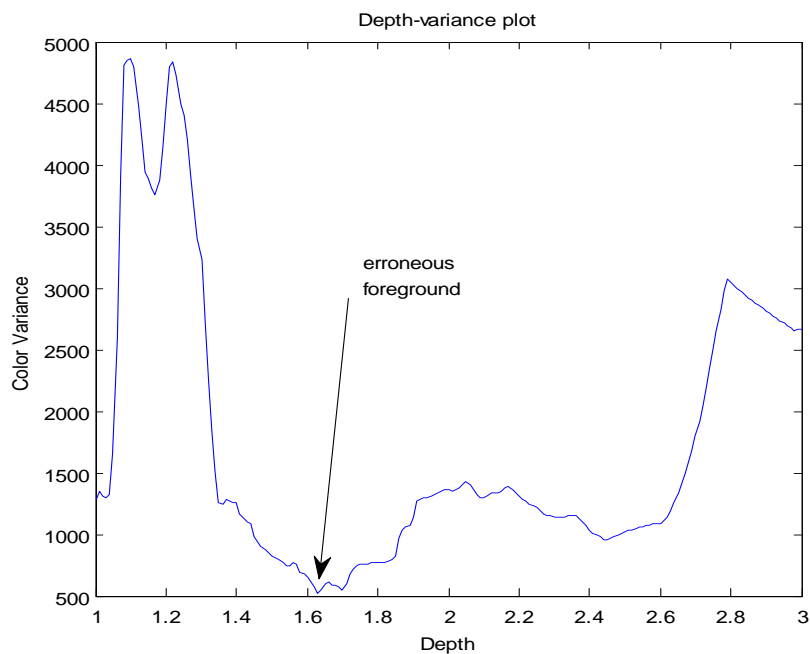
Both the variance and the number of effective cameras, as calculated in 14, are used as criterions in the selection of the depth. The number of effective cameras is used to prevent selection of depths for which very few cameras are considered inliers. This can happen in case the values are randomly distributed in the RGB space. Then the outlier removal method could choose one or two observations as inliers, having also a very low variance. This is general not the correct case so the selection of clusters with few members is stopped, in the following way.

Starting from the lowest depth, the first local minimum variance is selected and it is only replaced if a lower variance with a higher number of cameras is present for a higher depth. The reason that the scanning procedure starts from the lower depths to the higher ones is that we want to select the first visible object (foreground object) and not objects behind it.

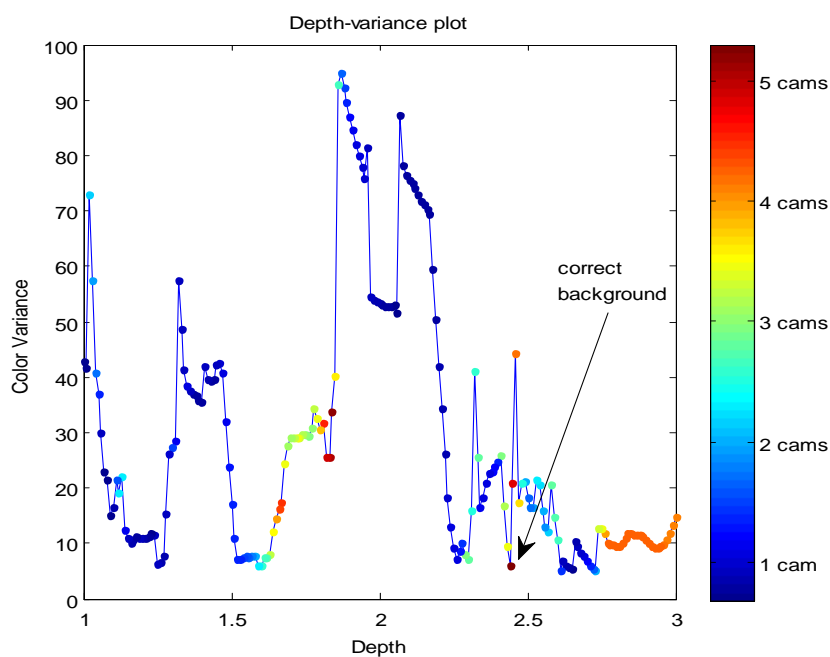
As an example, one pixel in the occluded area is considered. As it was already discussed in chapter 3.a and 3.b this pixel is the case that cannot be correctly generated with the basic or weighted approach. Even when the weights are considered, the selected depth is not correct (in the area of 1.6 m).



(a)



(b)



(c)

Figure 27: Depth-variance diagrams of a pixel in the occluded area. The diagrams are visualizations of the variance of the pixel for all the depths from 1m to 3m. (a) non-weighted variance, (b) weighted variance, (c) variance after the removal of outliers.

In the above diagram the blue line is the color variance diagram, after the outlier removal. The colorful dots indicate the effective number of cameras ( $N$ ). In this example the combination of a low variance and a high number of camera members happens for a depth around 2.4 meters. In this case the outlier removal method works for the occlusion problem.

There are still cases for which this approach would not work. When the majority of the cameras are viewing the wrong color, and the minority the correct, the outlier removal approach will consider inliers the wrong values. The real inliers will be excluded from the calculation of the final color of the pixel. In such a case that the correct values are excluded the result is worse than the one of the basic or the weighted approach.

#### 4. Experimental setup

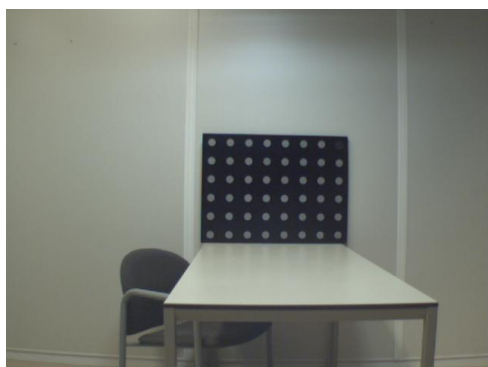
The presented experimental setup uses a pair-wise multi-view camera setup of 8 views, whereas the cameras are mounted without any geometric restrictions. Video frames are recorded at a resolution 640x480 at 15 fps.



Figure 28: Experimental setup.

Before the recording of the scene, the cameras were calibrated. The camera calibration step is an integral part of the process of 3D video acquisition. It is determining the internal camera geometric and optical characteristics (intrinsic parameters) and the 3D position and orientation of the camera frame relative to a world coordinate system (extrinsic parameters). This step is necessary to guarantee geometric consistency across the different terminals.

A calibration plate containing 47 dots was captured in four different positions and an minimum energy calibration algorithm, as proposed by Redert et al. at [33], was used.



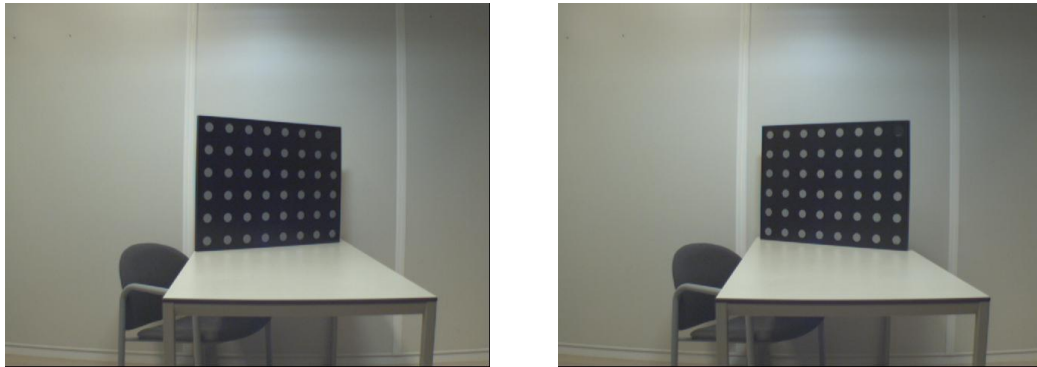
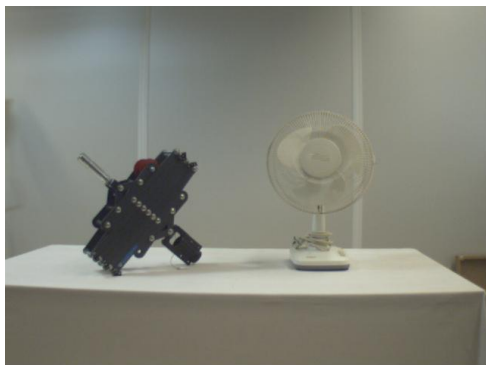


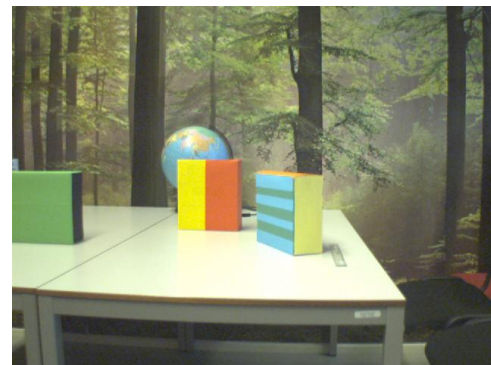
Figure 29: Calibration plate placed in four different positions for the calibration algorithm.

After the calibration step, each of the cameras captured one image from a different viewpoint. The recorded scene is stationary. The algorithm has been tested in stationary scenes; however it can be also used for video sequences. In this case each frame is reconstructed independently from the previous ones therefore the temporal characteristics of a video are not taken into account.

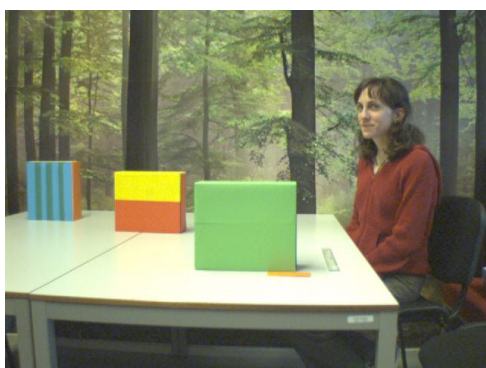
Different scenes were recorded, with different backgrounds, simple and more complex ones, people or just objects.



(a)



(b)



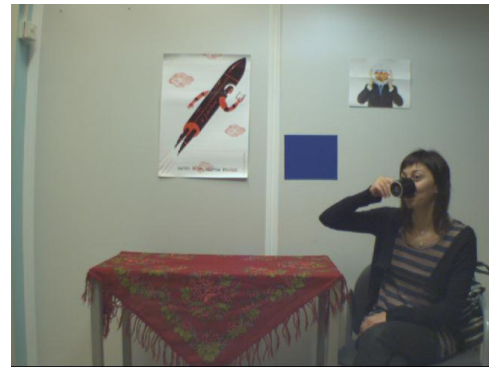
(c)



(d)



(e)



(f)



(g)



(h)

Figure 30: Captured scenes with different sceneries.

From the above scenes, two were selected to serve as the scenes in which the algorithms will be tested. A scene with a colorful, complex background and four boxes and a scene with a simple background and a human, were chosen. From now on the first scene is referred as *four boxes* scene (Figure 30.d), and the second one as *coffee* scene (Figure 30.g). In both scenes there are objects occluding the background or other objects so the handling of occlusions can be also assessed.

Professional lighting equipment was not used. The lighting of the room where the recordings took place is the normal ceiling lighting. Changes in illumination are present in the scene.

## 5. Evaluation

Objective evaluation of image and video quality is important for image processing systems. The quality assessment is by itself a wide research area, having as a goal to design algorithms for objective evaluation of quality in a way that is consistent with subjective human evaluation. By “consistent” it is meant that the algorithm’s assessment of quality should be in close agreement with human judgments, regardless of the type of distortion corrupting the image, the content of the image, or strength of distortion.

In the image coding and computer vision literature, the most frequently used measures are deviations between the original and coded images, with varieties of the mean square error (MSE) or signal-to-noise ratio (SNR) being the most common measures [34-36]. The reason for their widespread popularity is their mathematical tractability. However they do not necessarily correspond to all aspects of the observer’s visual perception of the errors, [34, 35], nor do they correctly reflect structural coding artifacts.

For multimedia applications, there has been an increase in the use of quality measures based on human perception [37-42]. Since a human observer is the end user in multimedia applications, an image quality measure that is based on a human vision model seems to be more appropriate for predicting user acceptance and for system optimization. This class of distortion measure in general gives a numerical value that will quantify the dissatisfaction of the viewer in observing the reproduced image in place of the original. The alternative is the use of subjective tests in which subjects view a series of reproduced images and rate them based on the visibility of the artifacts. Subjective tests are tedious, time consuming and expensive, and the results depend on various factors such as the observer’s background, motivation, etc., and actually only the display quality is being assessed.

An objective evaluation although not being the optimal one is usually part of the testing of an image processing technique. In this thesis, PSNR (peak signal-to-noise ratio) is used. The derivative signal to noise ratio, a criterion that considers the sensitivity of the human eye in the edge information is also computed. A subjective evaluation, based on the author’s visual interpretation is finally discussed.

Different approaches exist for computing PSNR of a color image. One simple approach is to calculate the metrics for the three R,G,B components and then average them. But, the human eye is most sensitive to intensity information. Therefore the image is first converted to a color space that separates the intensity channel, here YCbCr. The Y (luma), in YCbCr represents a weighted average of R, G, and B. G is given the most weight, again because the human eye perceives it most easily. With this consideration, the PSNR is computed only on the luma channel.

The PSNR, is calculated as follows:

$$PSNR = 10 \log_{10} \frac{255^2}{MSE} \quad (18)$$

where

$$MSE = \frac{\sum_{i,j} [I_o(i, j) - I_r(i, j)]^2}{M} \quad (19)$$

Where  $I_o[i,j]$  and  $I_r[i,j]$  are the intensity values at the  $(i,j)^{th}$  pixels of the original and reconstructed images respectively and  $M$  the number of pixels.

In order to compare the reconstructed views with the original images, the parameters of the virtual camera were set to the same values as one of the original cameras. For every virtual view the original view that coincides with it is excluded. Therefore in the evaluation part eight views are generated, using each time seven cameras. This influences a lot the PSNR values presented below. Especially in the weighted approach, excluding the closest in the virtual view camera deteriorates the final result.

The PSNR measure is computed for cropped images. The borders, not being captured from all the cameras, have been excluded from the evaluation as they are not representative. For images with dimensions  $500 \times 380$  these are the PSNR results:

4 boxes sequence



|                        | view 1 | view 2 | view 3 | view 4 | view 5 | view 6 | view 7 | view 8 |
|------------------------|--------|--------|--------|--------|--------|--------|--------|--------|
| <b>basic approach</b>  | 23.95  | 19.79  | 22.19  | 23.97  | 21.12  | 24.03  | 24.40  | 26.03  |
| <b>weighted</b>        | 25.19  | 22.91  | 24.85  | 28.62  | 22.14  | 26.033 | 27.39  | 28.03  |
| <b>outlier removal</b> | 23.52  | 21.78  | 24.78  | 26.62  | 21.37  | 23.88  | 25.23  | 25.94  |

Table I: PSNR for cropped images, 4 boxes scene (in dB)



|                        | view 1 | view 2 | view 3 | view 4 | view 5 | view 6 | view 7 | view 8 |
|------------------------|--------|--------|--------|--------|--------|--------|--------|--------|
| <b>basic approach</b>  | 21.15  | 16.60  | 20.25  | 20.52  | 20.18  | 19.60  | 22.62  | 23.66  |
| <b>weighted</b>        | 21.54  | 19.20  | 22.58  | 21.98  | 21.06  | 20.34  | 24.24  | 24.73  |
| <b>outlier removal</b> | 21.65  | 19.69  | 21.68  | 22.95  | 20.61  | 20.15  | 22.64  | 23.89  |

Table II: PSNR for non-cropped images, 4 boxes scene (in dB)

Coffee sequence



|                        | view 1 | view 2 | view 3 | view 4 | view 5 | view 6 | view 7 | view 8 |
|------------------------|--------|--------|--------|--------|--------|--------|--------|--------|
| <b>basic approach</b>  | 26.11  | 26.60  | 26.49  | 25.81  | 24.93  | 22.34  | 20.58  | 22.59  |
| <b>weighted</b>        | 29.14  | 29.37  | 27.56  | 26.60  | 29.14  | 24.13  | 21.15  | 23.66  |
| <b>outlier removal</b> | 27.51  | 27.92  | 26.69  | 26.09  | 26.53  | 23.29  | 21.24  | 23.05  |

Table III: PSNR for cropped images, coffee scene (in dB)



|                        | view 1 | view 2 | view 3 | view 4 | view 5 | view 6 | view 7 | view 8 |
|------------------------|--------|--------|--------|--------|--------|--------|--------|--------|
| <b>basic approach</b>  | 21.15  | 24.55  | 21.07  | 25.85  | 24.91  | 16.49  | 18.61  | 19.32  |
| <b>weighted</b>        | 21.82  | 25.56  | 21.49  | 26.85  | 27.21  | 16.77  | 19.07  | 19.90  |
| <b>outlier removal</b> | 23.78  | 25.09  | 23.67  | 26.35  | 25.89  | 16.66  | 19.08  | 20.55  |

Table IV: PSNR for non-cropped images, coffee scene (in dB)

The results of the cropped images have a higher PSNR as it was expected. For both sequences the weighted approach has the best performance. The outlier removal method does not enhance the quality of the final images in general. For a couple views the outlier removal method has a higher PSNR than the weighted approach and for other views lower than the basic approach. The performance of the methods depends on the scenery and as it was explained in chapter 3.c there are cases that the removal of the outlier can deteriorate the final result.

Another remark is that when the whole image is evaluated the outlier removal method has better metrics than the basic and the weighted approach. The method handles better the generation of the borders of the images, but this is not indicative of its general behaviour.

Yalazan et al.,[43] are proposing the derivative signal to noise ratio as an objective fidelity criterion which considers the sensitivity of the human eye to the edge information. Human eye uses edge information while perceiving an image. The authors claim that the new criterion should be sensitive to regions of fast changes (edges) in an image in order to agree with subjective decisions.

$$Derivative\ SNR = \frac{10 \log_{10} \sum_{i,j} I'_o(i, j)^2}{\sum_{i,j} (I'_o(i, j) - I'_r(i, j))^2} \quad (20)$$

Where  $I'_o(i, j)$  and  $I'_r(i, j)$  are approximate gradients at the  $(i,j)^{th}$  pixel of the original and reconstructed images respectively, which are calculated as:

$$I'(i, j) = |I(i, j) - I(i + 1, j)| + |I(i, j) - I(i, j + 1)| \quad (21)$$

The last row and last column are not used in the calculation of derivative SNR since the above equation cannot be applied to those pixels. The equation computes the horizontal and vertical changes at each pixel, hence the edge information is emphasized. In other words  $I(i,j)$  extracts the high frequency components of the image. When a reconstruction process is not much successful in reproducing the edges of the original image, the noise term in the denominator of the equation gets large resulting in a poor value of the derivative SNR. The derivative SNR criterion which emphasizes the contribution from the high frequency region is expected to be more correlated to subjective decisions because of its similarity to the perceptual mechanism of the human eye.

#### 4 boxes sequence

|  | view 1 | view 2 | view 3 | view 4 | view 5 | view 6 | view 7 | view 8 |
|--|--------|--------|--------|--------|--------|--------|--------|--------|
| <b>basic approach</b><br>( $\times 10^{-5}$ )  | 0.26   | 0.19   | 0.12   | 0.19   | 0.14   | 0.18   | 0.24   | 0.25   |
| <b>weighted</b><br>( $\times 10^{-5}$ )        | 0.27   | 0.19   | 0.14   | 0.20   | 0.15   | 0.17   | 0.24   | 0.25   |
| <b>outlier removal</b><br>( $\times 10^{-5}$ ) | 0.18   | 0.10   | 0.10   | 0.14   | 0.11   | 0.11   | 0.13   | 0.15   |

Table V: Derivative SNR for cropped images, 4 boxes sequence (in dB)

Coffee sequence

|  | view 1 | view 2 | view 3 | view 4 | view 5 | view 6 | view 7 | view 8 |
|--|--------|--------|--------|--------|--------|--------|--------|--------|
| <b>basic approach</b><br>( $\times 10^{-5}$ )  | 0.21   | 0.31   | 0.20   | 0.31   | 0.27   | 0.19   | 0.19   | 0.18   |
| <b>weighted</b><br>( $\times 10^{-5}$ )        | 0.21   | 0.33   | 0.21   | 0.28   | 0.35   | 0.18   | 0.17   | 0.18   |
| <b>outlier removal</b><br>( $\times 10^{-5}$ ) | 0.15   | 0.21   | 0.18   | 0.19   | 0.18   | 0.11   | 0.09   | 0.14   |

Table VI: Derivative SNR for cropped images, coffee sequence (in dB)

The values of the derivative SNR highlight the fact that the outlier removal method is the least visually acceptable. As it is going to be discussed in the subjective evaluation, the outlier removal method gives non-smoothed images and this irritates the visual perception.

In order to evaluate subjectively the methods, the results on Appendix A are used. The virtual views regenerated from the basic approach are visually acceptable taking into account that the method remains quite simple and fast. To have a better insight, the scene under consideration can be divided into different parts. The borders of the images, where there are artifacts, should be excluded from the evaluation phase.

In the first scene, the background is highly textured. The background in the regenerated images keeps the high texture. The white table is a homogeneous area at the original views except few pixels due to illumination changes; in general the reconstructed table has a smooth view. The problem with this approach is located in the area around the boxes and especially between the two boxes at the right (the purple and the striped one). Part of background that should be visible is erroneously reconstructed.

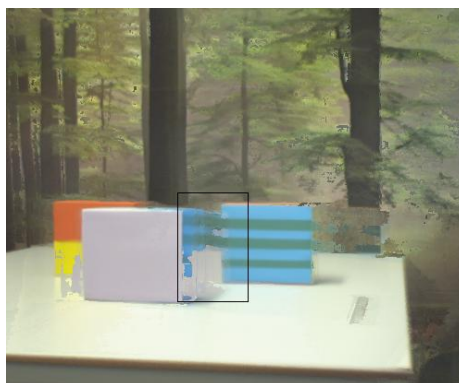


Figure 31: A virtual view generated by the basic approach.

When the camera proximity weights are integrated in the method the generated virtual views are better. The improvement is visible especially for the last virtual views, where the occlusion problem is present.

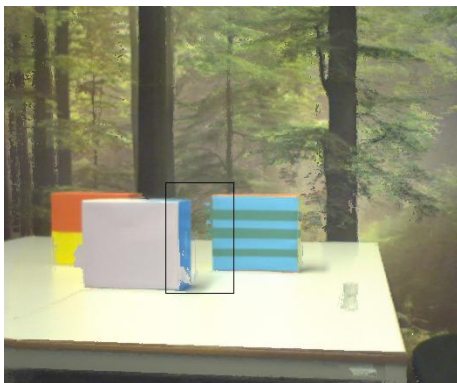


Figure 32: A virtual view generated by the weighted approach.

The quality of the images generated by the outlier removal method seems to deteriorate in comparison with the weighted approach. A grain effect is visible especially in homogeneous areas like the table. The camera values are not averaged, some of them are not participating in the calculation of the color of the pixel. This has as a consequence that the surfaces are less smooth. The occlusions are handled well, and this was expected since the proximity weights are used as well.



Figure 33: A virtual view generated by the outlier removal approach

The *coffee* sequence, has a smooth simple background, and does not include a highly occluded area. The results for this sequence are visually better. The basic approach gives a bit blurred images, but the other two methods seem to work efficiently.

## 6. Discussion and Future work

The goal of the research of this thesis was to study the feasibility of a simple algorithm to create 3D content for 3DTV applications. The requirements of a 3DTV application for a whole scene video with editing capabilities and high quality, and the constraints imposed by the number of the available cameras formulate the research area.

First the state of the art methods were investigated. There are two main categories, as it was discussed in detail in chapter two. The model-based approaches, using complex geometry models of the scene. Synthetic videos, using blue-screen as a background for example, can be generated with such techniques but their complexity makes their use prohibitive for the generation of a video of the whole scene. The other category, image-based approaches, is able to reconstruct 3D videos for whole scenes and that is that makes it more promising for 3DTV applications. The dense sampling of the scene that is required complicates its use.

Current methods cannot work efficiently without imposing a lot of limitations. That was the motivation of this thesis. We investigated a new approach that uses per-pixel operations to allow for parallel computations, scalability and flexibility. For each pixel to be rendered a depth hypothesis was generated. It was solved by projecting the pixel in the camera planes and comparing the color values. The algorithm worked properly, with some exceptions, e.g. areas with occlusion. To overcome the occlusion problem camera proximity weights were assigned to the cameras. The distance between the position of the virtual and original camera was calculated. Original cameras closer to the camera view were assigned a greater weight. The improvement in the visual quality of the generated images was significant.

However artifacts were still present. Investigation of the RGB values of the eight cameras for one pixel, indicated that there were different reasons for which the camera agreement hypothesis for the correct depth was not true. An occlusion for example is a potential cause for outlier values in the RGB dataset. To solve the outlier problem we investigated two approaches, a non-weighted outlier removal and a weighted outlier removal method. The generated images are not visually better in comparison with the ones generated with the basic approach. However for some special areas the outlier removal method works properly. So, integration of more sophisticated criteria in the depth selection stage may lead to better results.

The methods discussed have the advantage that can generate a 3D video of the whole scene while they keep the computational complexity of the system low and have as input only eight original images. They can directly benefit by using more cameras or cameras with higher resolution in order to enhance the final result.

The fact that there is no intermediate representation, adds on the freedom of the adopted methods but on the other hand any inter-view relations are not taken into account. Every time a new virtual view is generated the analysis stage has to run.

To sum up, after analyzing in detail the behavior of pixels in the reconstruction stage we gained a very good insight of their behavior. This information was incorporated in the approaches tested. The results are very promising. Some improvements can be made. The scenery for example can be segmented in areas according to their special characteristics (e.g. occluded areas, objects at the front). Then each segment could be regenerated by a different approach according to its special characteristics. The depth maps of the generated images, (Appendix C) could be used as an indicator of which areas need special attention. In Appendix B, a clustering experiment highlights the fact that the special characteristics within an area of the image are spatial consistent.

## **b. Future Research**

Layered Depth Images are used widely for rendering 3D objects. Our approach could be extended to more than one layer. The per-pixel analysis facilitates the generation of layers from the original images. Preliminary experiments were conducted in which the layers were selected as modes of the color variance. The depth with minimum color variance was considered as the first layer, the depth with the second minimum variance the second one.

The spatial and temporal connectivity, both present in sequence of images, were not taken into account. In a future research their use could enhance for example the non-smooth result of the outlier removal method.

## 7. Appendix

### A. Results

#### *Four boxes sequence*

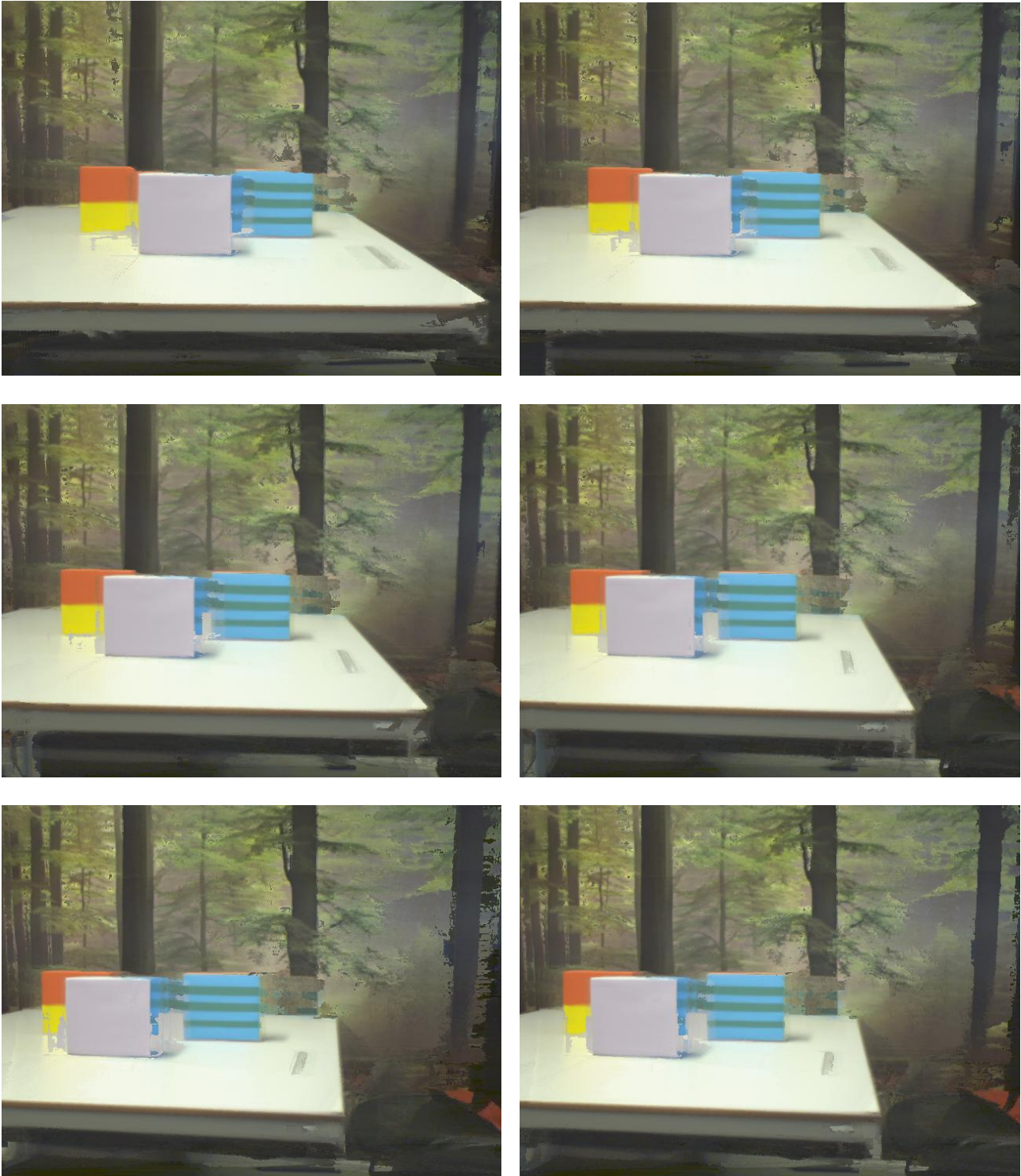


*Figure 34: Six of the virtual views for the 4 boxes sequence generated with the basic approach. The positions of the virtual cameras are shown in figure 40.*

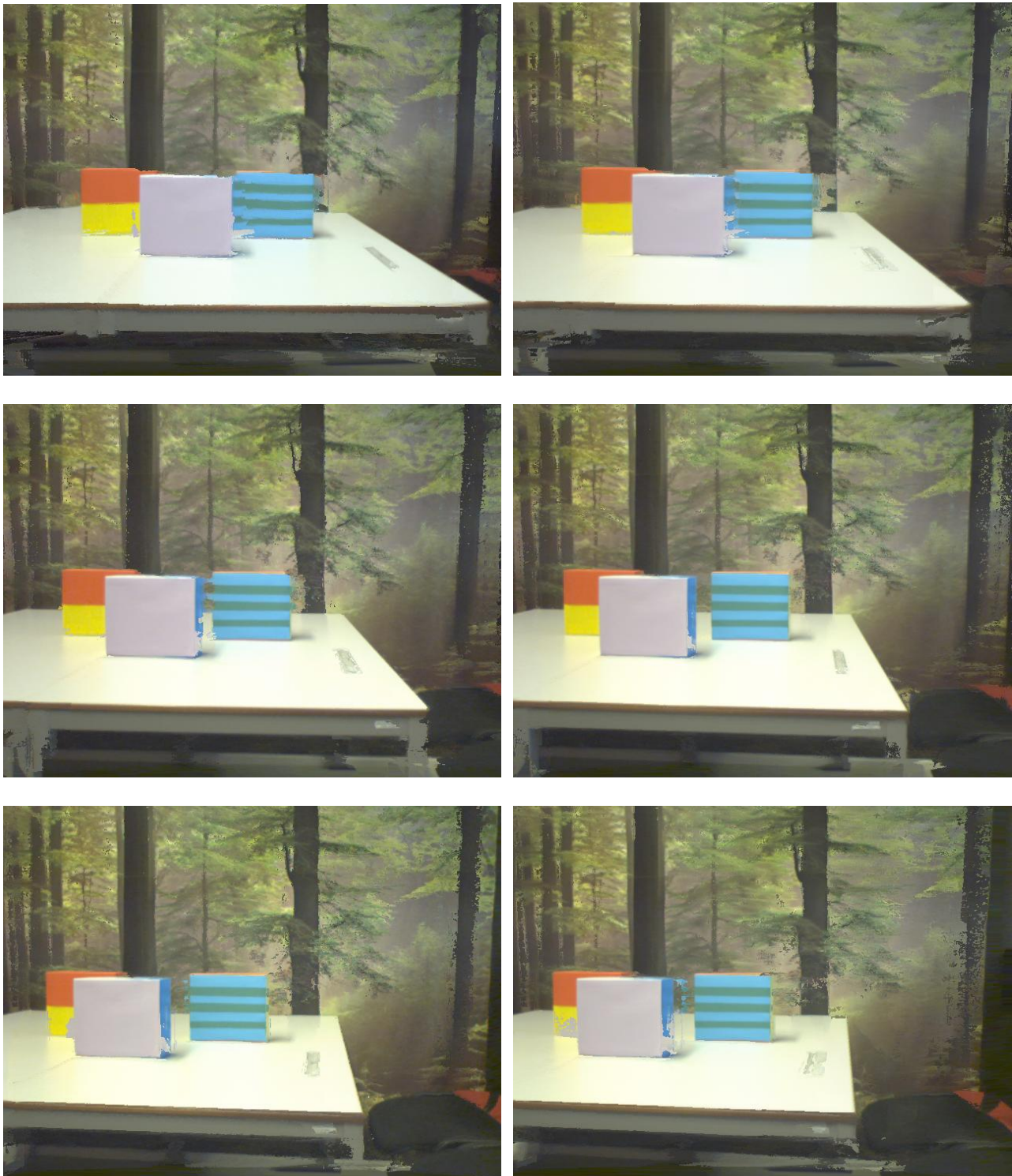


Figure 35: Six of the virtual views for the 4 boxes sequence generated with the weighted approach.

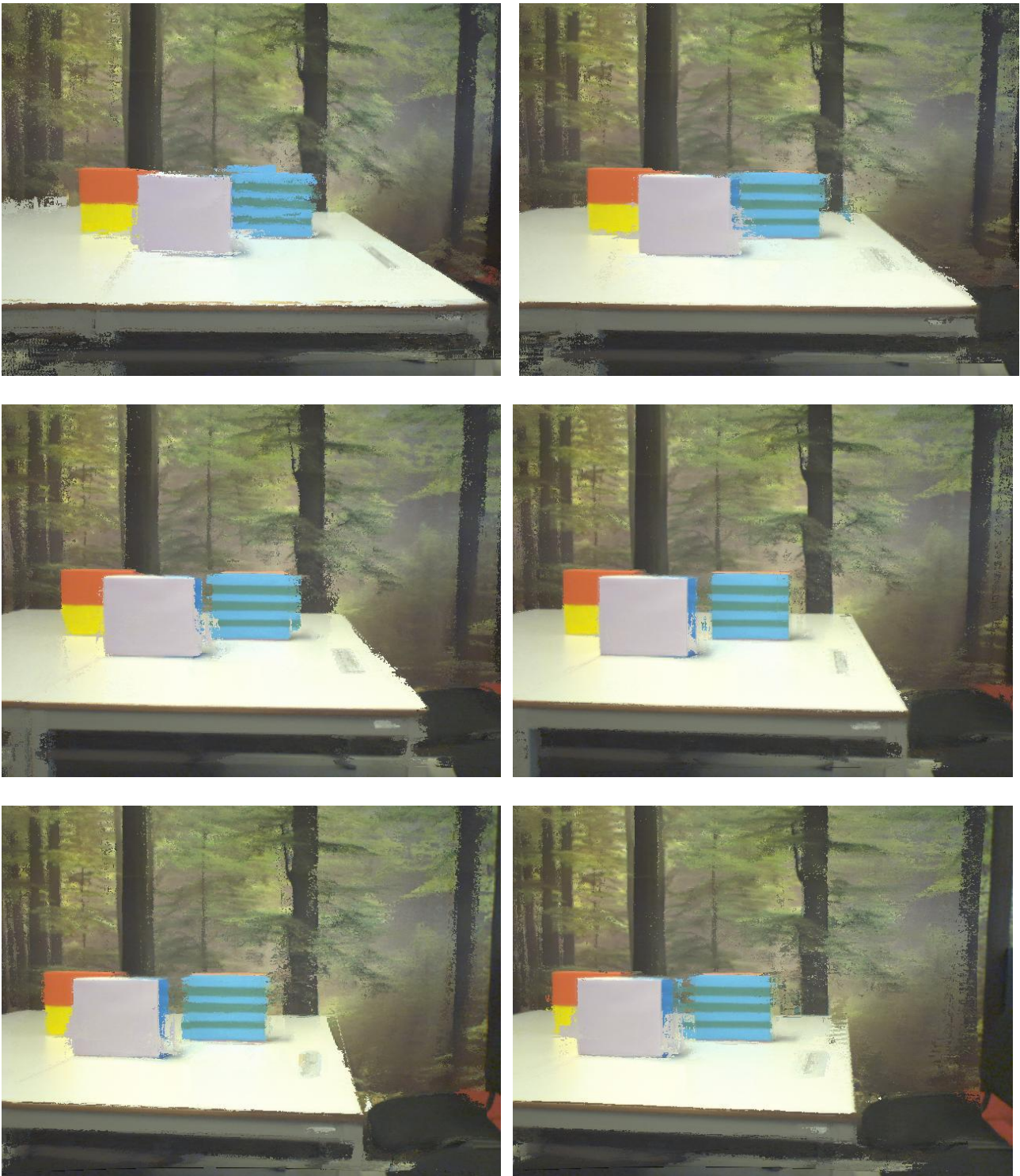


Figure 36: Six of the virtual views for the 4 boxes sequence generated with the outlier removal approach.

*coffee sequence*



*Figure 37: Six of the virtual views for the coffee sequence generated with the basic approach.*



Figure 38: Six of the virtual views for the coffee sequence generated with the weighted approach.



Figure 39: Six of the virtual views for the coffee sequence generated with the outlier removal approach.

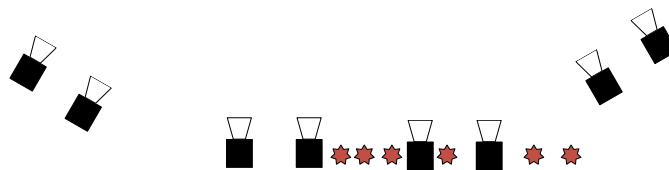


Figure 40: The red stars are indicating the positions of the six virtual views shown in the previous figures, in relevance to the original cameras configuration.

## B. Clustering experiment

Here, a pixel is considered, and the outlier removal algorithm is iterated eight times, having as a starting point,  $V_c$ , one of the vectors containing the RGB information for one of the cameras each time. The dataset of the algorithm are the eight  $V_c$  vectors. For the different iteration points the algorithm outputs different mean values.

Then the eight different mean values are compared, and values with distance less than a threshold are combined. In this way the possibility of different clusters or single outlier values within the dataset of the eight  $V_c$  vectors is investigated. The purpose of this experiment is to test in areas with different characteristics what camera clusters are generated for different depths. The spatial consistency of these results is also investigated.

In the following diagram, one pixel in the front part of the *four boxes* sequence is considered, and the clusters found for every depth are visualized. The blue line is the variance of all the eight cameras as a function of depth calculated with the basic approach as discussed in section 3.a. The 'x' represents one cluster, its y value indicates the variance of the cluster and finally the color stands for the number of the cameras participating in the cluster. This figure corresponds to one pixel in the front part of the image, on the table. It can be noticed easily that for the correct depth, around 1.4 meters, all the eight cameras are in agreement. Therefore there are no outliers.

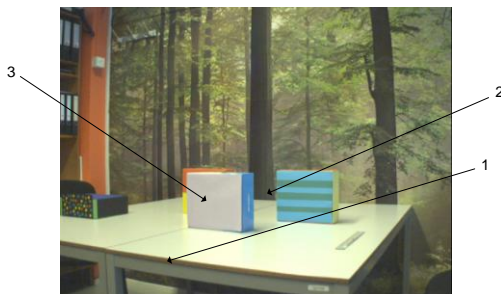


Figure 41: Position of the three pixels discussed in this section

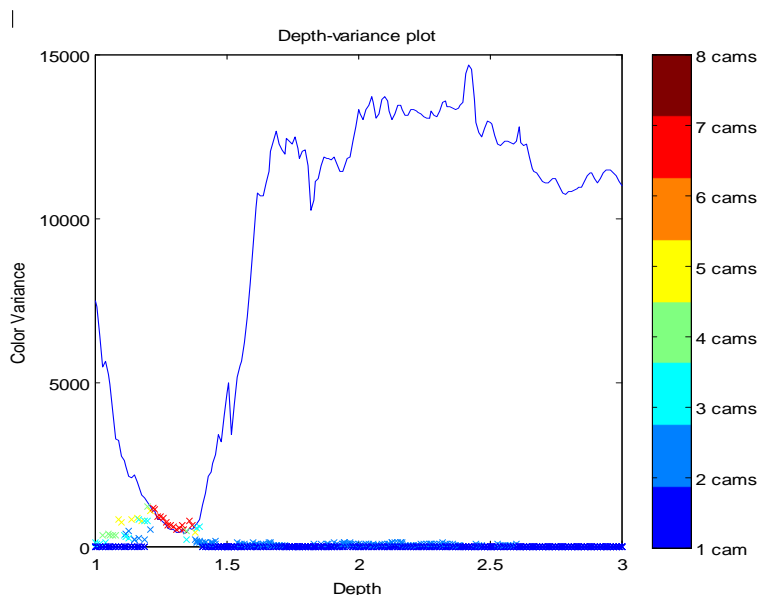


Figure 42: Depth –color variance plot. The ‘x’ symbol stands for a cluster of cameras. Its color indicates the number of the members of the cluster, its height the variance of the cluster. For a pixel in the front part of the image (Figure 20), all the eight cameras are in agreement for the correct depth.

To check the consistency of the clustering between neighboring pixels, the clustering algorithm now is performed in more pixels, sequential in the x axis. Only the biggest cluster of each depth is plotted in the next diagram.

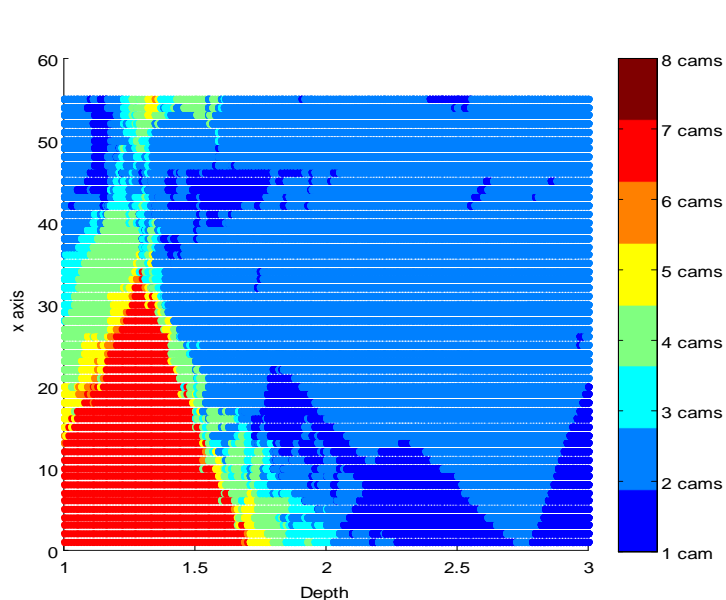


Figure 43: The number of camera members of a cluster is indicated by the color of the x symbol. 40 pixels successive in the x axis are considered.

A pixel in the occluded area is now considered. The created clusters comprise of 1-3 cameras highlighting the fact that the cameras are distracted by occlusion. The same holds for neighboring pixels.

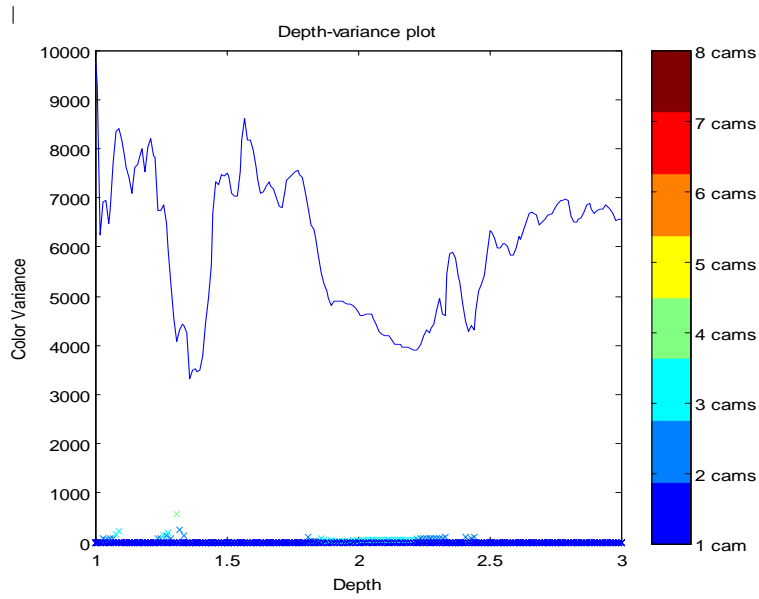


Figure 44: Depth –color variance plot. The ‘x’ symbol stands for a cluster of cameras. Its color indicates the number of the members of the cluster, its height the variance of the cluster. For a pixel in the occlusion area (Figure 27), the cameras are not in agreement and they are forming separated small clusters.

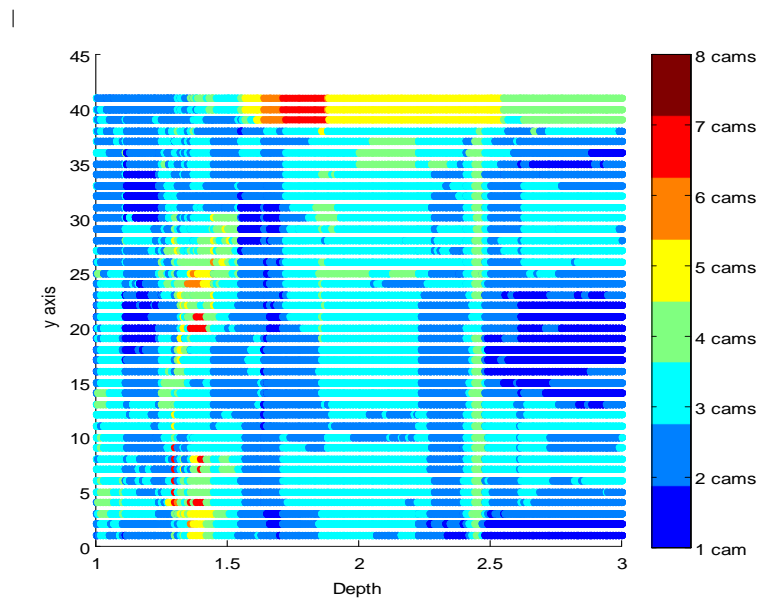


Figure 45: The number of camera members of a cluster is indicated by the color of the x symbol. 40 pixels successive in the y axis are considered.

A pixel in the box positioned in the middle of the table is considered. The cameras are in agreement but for a wide range of depths (Figure 46).

The clustering is performed for neighboring pixels, in both axis x and y (Figures 47 and 48). It can be noticed that within this neighborhood of pixels, the number of camera members is consistent for similar depths.

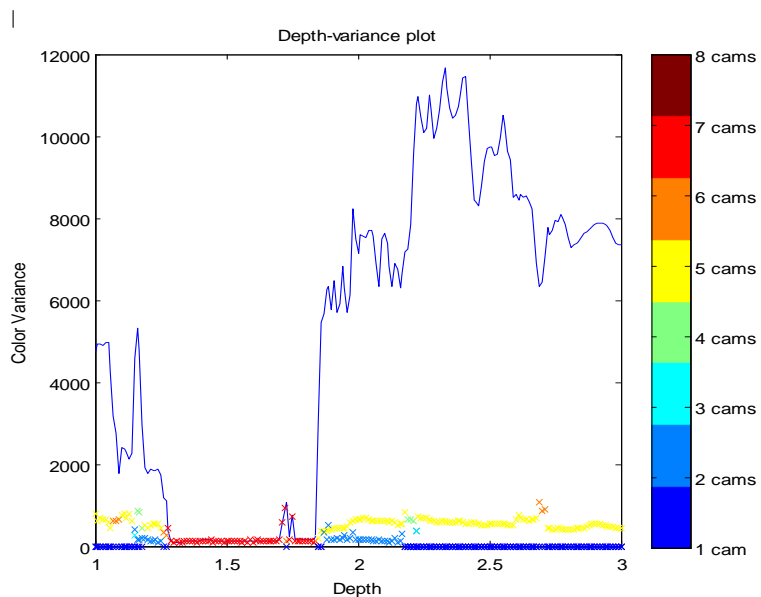


Figure 46: Depth –color variance plot. The 'x' symbol stand for a cluster of cameras. Its color indicates the number of the members of the cluster, its height the variance of the cluster. For a pixel on the box, the cameras are in agreement for a wide area of depths.

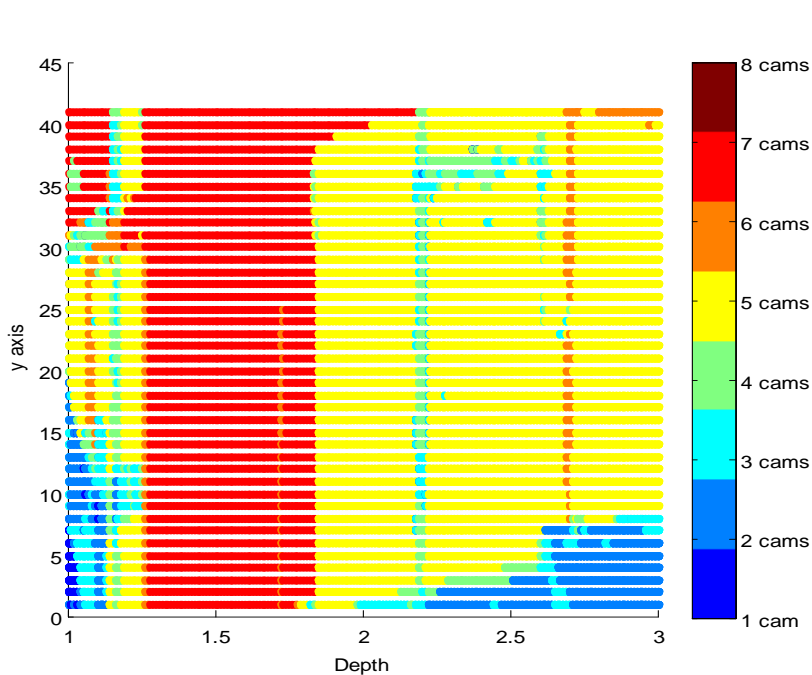


Figure 47: The number of camera members of a cluster is indicated by the color of the x symbol. 40 pixels successive in the y axis are considered.

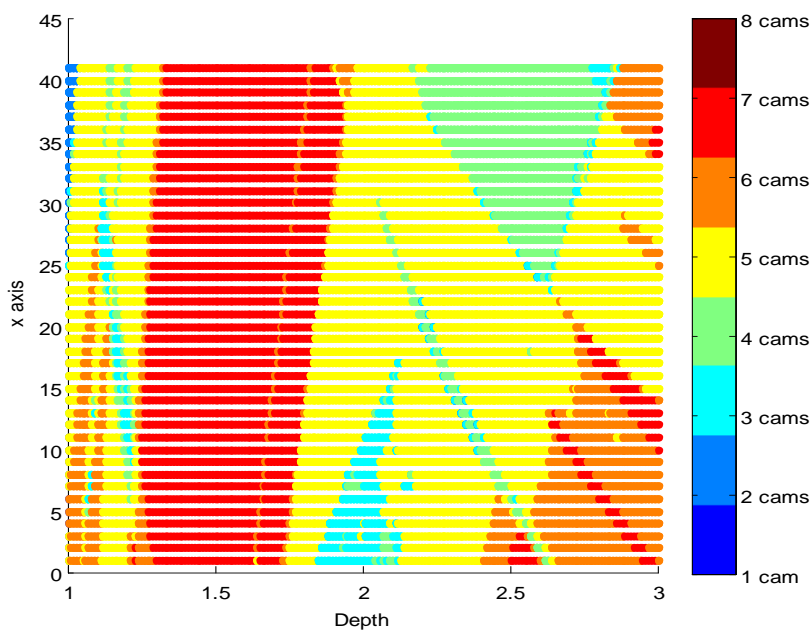


Figure 48: The number of camera members of a cluster is indicated by the color of the x symbol. 40 pixels successive in the x axis are considered.

### C. Depth maps

Our approach when reconstructing a virtual view is implicitly reconstructing its depth map. Three depth maps are shown here reconstructed by the basic, the weighted and the outlier removal approach respectively.

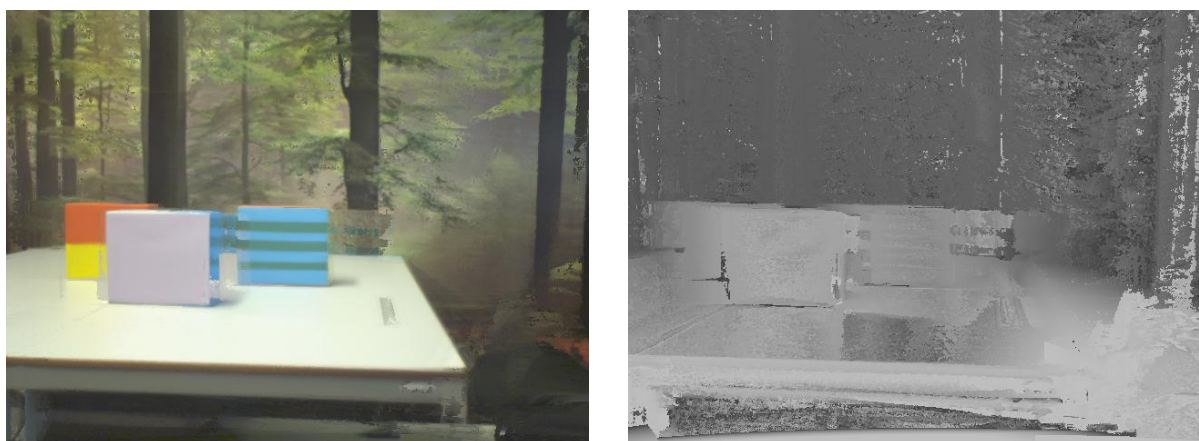


Figure 49: virtual view and its depth map reconstructed with the basic approach.

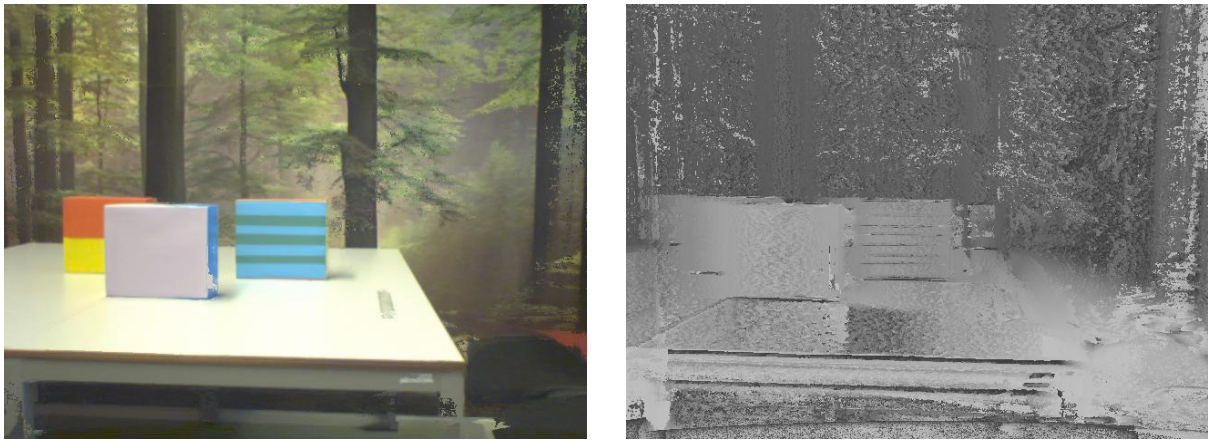


Figure 50: virtual view and its depth map reconstructed with the weighted approach.

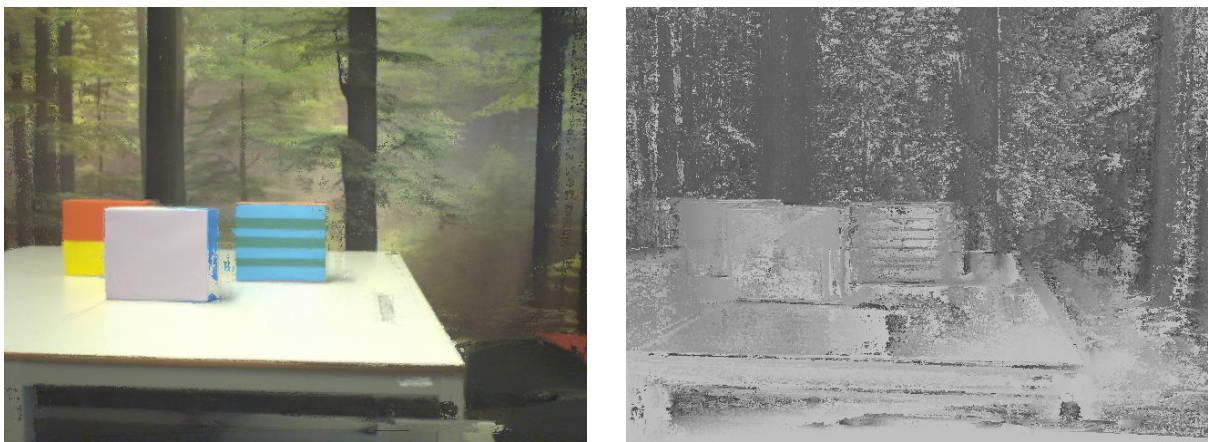


Figure 51: virtual view and its depth map reconstructed with the outlier removal approach.

### D. Mean Shift algorithm

Mean shift which was proposed in 1975 by Fukunaga and Hostetler [44], is a nonparametric, iterative procedure that shifts each data to local maximum of density function.

An intuitive description of the mean shift algorithm is shown in Figure 36. Given a set of data points, the objective is to find the densest region.

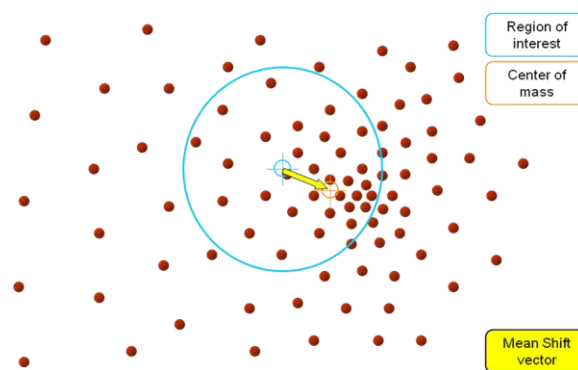


Figure 40: Intuitive description of mean shift algorithm. In the above distribution of identical billiard balls, the objective is to find the densest region.

The mean shift algorithm does not require prior knowledge of the number of clusters, and does not constraint the shape of clusters.

Given  $\{ x_i \}_{i=1, \dots, n}$  an arbitrary set of  $n$  points in the  $d$ -dimensional Euclidean space  $\mathbb{R}^d$ . The multivariate kernel density estimate obtained with kernel  $K(x)$  and a symmetric positive,  $d \times d$ , bandwidth matrix  $H$ , computed in the point  $x$  is given by,(22):

$$\hat{f}(x) = \frac{1}{n} \sum_{i=1}^n K_H(x - x_i) \tag{22}$$

where

$$K_H(x) = |H|^{-1/2} K(H^{-1/2}x) \tag{23}$$

The  $d$ -variate kernel  $K(x)$  is a bounded function satisfying:

$$\begin{aligned} \int_{\mathbb{R}^d} K(x) dx &= 1 & \lim_{\|x\| \rightarrow \infty} \|x\|^d K(x) &= 0 \\ \int_{\mathbb{R}^d} xK(x) dx &= 0 & \int_{\mathbb{R}^d} xx^T K(x) dx &= c_K I \end{aligned} \tag{24}$$

where  $c_K$  is a constant.

A special class of radially symmetric kernels satisfying:

$$K(x) = c_{k,d} k(\|x\|^2) \tag{25}$$

is of interest in the work of Comaniciu et al.,[45], where  $k(\cdot)$  is called the profile of the kernel and  $c_{k,d}$  is a normalization constant.

Employing a fully parameterized  $H$  increases the complexity of the estimation. Employing only one bandwidth parameter, the kernel density estimator (1) becomes:

$$\hat{f}(x) = \frac{1}{nh^d} \sum_{i=1}^n K\left(\frac{x - x_i}{h}\right) \tag{26}$$

Employing the profile notation, the density estimator (26) can be rewritten as:

$$\hat{f}_{h,K}(x) = \frac{c_{k,d}}{nh^d} \sum_{i=1}^n k\left(\left\|\frac{x - x_i}{h}\right\|^2\right) \tag{27}$$

The first step in the analysis of a space with the underlying density  $f(x)$  is to find the modes of this density. The modes are located among the zeros of the gradient  $\nabla f(x) = 0$  and the mean shift procedure is an way to locate these zeros without estimating the density.

The density gradient estimator obtained as the gradient of the density estimator:

$$\hat{\nabla} f_{h,K}(x) = \nabla \hat{f}_{h,K}(x) = \frac{2c_{k,d}}{nh^{d+2}} \sum_{i=1}^n (x - x_i) k' \left( \left\| \frac{x - x_i}{h} \right\|^2 \right) \quad (28)$$

The function  $g(x) = -k'(x)$  is defined, assuming that the derivative of the kernel profile exists for all  $x \in [0, \infty]$ , except for a finite set of points. Using  $g(x)$  for profile, the kernel  $G(x)$  is defined as:

$$G(x) = c_{g,d} g \left( \|x\|^2 \right) \quad (29)$$

Where  $c_{k,d}$  is the corresponding normalization constant. The kernel  $K(x)$  was called the shadow of  $G(x)$ . The Epanechnikov kernel is the shadow of the uniform kernel, while the normal kernel and its shadow have the same expression.

Introducing  $g(x)$  into (28), yields

$$\hat{\nabla} f_{h,K}(x) = \frac{2c_{k,d}}{nh^{d+2}} \sum_{i=1}^n (x_i - x) g \left( \left\| \frac{x - x_i}{h} \right\|^2 \right) = \frac{2c_{k,d}}{nh^{d+2}} \left[ \sum_{i=1}^n g \left( \left\| \frac{x - x_i}{h} \right\|^2 \right) \right] \left[ \frac{\sum_{i=1}^n x_i g \left( \left\| \frac{x - x_i}{h} \right\|^2 \right)}{\sum_{i=1}^n g \left( \left\| \frac{x - x_i}{h} \right\|^2 \right)} - x \right] \quad (30)$$

where  $\sum_{i=1}^n g \left( \left\| \frac{x - x_i}{h} \right\|^2 \right)$  is assumed to be a positive number. This condition is easy to satisfy for all the

profiles met in practice. Both terms of the product in (30) have special significance. From (27), the first term is proportional to the density estimate at  $x$  computed with the kernel  $G$ .

$$\hat{f}_{h,K}(x) = \frac{c_{k,d}}{nh^d} \sum_{i=1}^n g \left( \left\| \frac{x - x_i}{h} \right\|^2 \right) \quad (31)$$

The second term is the mean shift

$$m_{h,G}(x) = \left[ \frac{\sum_{i=1}^n x_i g\left(\left\|\frac{x-x_i}{h}\right\|^2\right)}{\sum_{i=1}^n g\left(\left\|\frac{x-x_i}{h}\right\|^2\right)} - x \right] \quad (32)$$

i.e. the difference between the weighted mean, using the kernel  $G$  for weights, and  $x$ , the center of the kernel(window). From (31) and (32), (30) becomes

$$\hat{\nabla} f_{h,K}(x) = \hat{f}_{h,G}(x) \frac{2c_{k,d}}{nh^{d+2}} m_{h,G}(x) \quad (33)$$

yielding

$$m_{h,G}(x) = \frac{1}{2} h^2 c \frac{\hat{\nabla} f_{h,K}(x)}{\hat{f}_{h,G}(x)} \quad (34)$$

The expression (34) shows that, at location  $x$ , the mean shift vector computed with kernel  $G$  is proportional to the normalized density gradient estimate obtained with kernel  $K$ . The normalization is by the density estimate in  $x$  computed with the kernel  $G$ .

The relation captured in (34) is intuitive; the local mean is shifted toward the region in which the majority of the points reside. Since the mean shift vector is aligned with the local gradient estimate, it can define a path leading to a stationary point of the estimated density. The modes of the density are such stationary points. The mean shift procedure, obtained by successive

- Computation of the mean shift vector  $m_{h,G}(x)$
- Translation of the kernel (window)  $G(x)$  by  $m_{h,G}(x)$

will converge at a nearby point where the estimate has zero gradient.

## 8. References

- [1] W.Matusik, H. Pfister, *3D TV: a scalable system for real-time acquisition, transmission, and autostereoscopic display of dynamic scenes*, International Conference on Computer Graphics and Interactive Techniques archive ACM SIGGRAPH 2004
- [2] A.Kubota, A. Smolic, M. Magnor, M. Tanimoto, Ts. Chen, Ch. Zhang, *Multiview Imaging and 3DTV*, Signal Processing Magazine IEEE, v.24, issue(6), 2007
- [3] Wilburn, B., N. Joshi, V. Vaish, E.-V. Talvala, E. Antunez, A. Barth, A. Adams, M. Horowitz, and M. Levoy: 2005, *High performance imaging using large camera arrays*, Proceedings of SIGGRAPH (ACM Transactions on Graphics) 24(3), 765–776.
- [4] Zitnick, C. L., S. B. Kang, M. Uyttendaele, S.Winder, R. Szeliski, *High-quality video view interpolation using a layered representation*, Proceedings of SIGGRAPH (ACM Transactions on Graphics) 2004, pp. 600–608.
- [5] Kanade, T., P. W. Rander, P. J. Narayanan: 1997, *Virtualized Reality: Constructing virtual worlds from real scenes*, IEEE MultiMedia Magazine 1(1), 34–47.
- [6] L.Onural, Th.Sikora, J.Ostermann, A.Smolic, M.R.Civanlar, J.Watson, *An Assessment of 3DTV Technologies*, 2006 NAB BEC Proceedings
- [7] M. op den Beeck, A. Redert, *Three dimensional video for the home*, Proceedings of EUROIMAGE ICAV3D 2001, International Conference on Augmented, Virtual Environments and Three-Dimensional Imaging, Mykonos, Greece, May 30 – June 1, 2001, pp. 188-191
- [8] R. Börner, B. Duckstein, O. Machui, R. Röder, T. Sinning and T. Sikora, *A family of single-user autostereoscopic displays with head-tracking capabilities*, IEEE Transactions on Circuits and Systems for Video Technology, Vol. 10, No. 2, pp. 234- 243, 2000
- [9] Philips lenticular screens, [http:// www.research.philips.com/generalinfo/special/3dlcd](http://www.research.philips.com/generalinfo/special/3dlcd)
- [10] J. Carranza, C. Theobalt, M. Magnor, H.-P. Seidel, *Free-viewpoint video of human actors*, in Proc. ACM Conf. Comput. Graph. (SIGGRAPH'03), 2003, pp. 569–577.

- [11] C. Theobalt, N. Ahmed, G. Ziegler, H. Seidel, *High-Quality Reconstruction from Multiview Video Streams, Dynamic representation of 3-D human actors*, Signal Processing Magazine IEEE, v.24, issue(6), 2007
- [12] T. Matsuyama, X. Wu, T. Takai, T. Wada, *Real-Time Dynamic 3-D Object Shape Reconstruction and High-Fidelity Texture Mapping for 3-D Video*, IEEE Transactions on Circuits and Systems for Video Technology, vol.14, no.3, March 2004.
- [13] S. Vedula, S. Baker, T. Kanade, *Spatio-temporal view interpolation*, In: EGRW '02, pp. 65-76, 2002
- [14] T. Fujii, T. Kimoto, M. Tanimoto, *Ray space coding for 3D visual communication*, Picture Coding Symp. 1996, Mar. 1996, pp. 447–451.
- [15] M. Levoy, P. Hanrahan, *Light field rendering*, in Proc. ACM SIGGRAPH, Aug. 1996, pp. 31–42.
- [16] H.Y. Shum, L.W. He, *Rendering with concentric mosaics*, in Proc. ACM SIGGRAPH, Aug. 1999, pp. 299–306.
- [17] E.H. Adelson, J.R. Bergen, *The plenoptic function and the elements of early vision*, In Computational Models of Visual Processing, Landy and Movshon, Eds. MIT Press, Cambridge, Massachusetts, 1991, ch. 1.
- [18] L. McMillan and G. Bishop, *Plenoptic modeling: an image-based rendering system*, in Proc. Comput. Graphics (SIGGRAPH '95), 1995, pp. 39–46.
- [19] S.J. Gortler, R. Grzeszczuk, R. Szeliski, and M.F. Cohen, *The Lumigraph*, in Proc. ACM SIGGRAPH'96, Aug. 1996, pp. 43–54
- [20] C. Fehn, P. Kauff, M. Op de Beeck, F. Ernst, W. Ijsselsteijn, M. Pollefeys, L. Vangool, E. Ofek, I. Sexton, *An evolutionary and optimised approach on 3DTV*, IBC 2002, Int. Broadcast Convention, Amsterdam, Netherlands, Sept. 2002
- [21] P. Debevec, C. Taylor, J. Malik, *Modeling and rendering architecture from photographs: A hybrid geometry- and image-based approach*, in Proc. SIGGRAPH 1996, 1996, pp. 11–20.
- [22] S. Wurmlin, E. Lamboray, M. Gross, *3D video fragments: Dynamic point samples for real-time free-viewpoint video*, Comput. Graph., (Special issue on coding, compression and streaming techniques for 3D and multimedia data), vol.28, no. 1, pp. 3–14, 2004.

- [23] M. Waschbusch, St.Wurmlin, D. Cotting, F. Sadlo, M. Gross, *Scalable 3D Video of Dynamic Scenes*, the Visual Computer 21(8-10):629-638, 2005
- [24] A. Broadhurst, T. Drummond, R. Cipolla, *A probabilistic framework for the space carving algorithm*, In: ICCV '01, pp. 388-393 (2001)
- [25] <http://graphics.ethz.ch/research/3dvideo/>
- [26] J. Shade, S. Gortler, L. Hey, and R. Szeliski, "*Layered depth images*," in Proceedings of ACM SIGGRAPH'98, Orlando, Florida, 1998, pp. 231–242.
- [27] S. M. Seitz, C. R. Dyer, *Photorealistic scene reconstruction by voxel coloring*, in Proceedings of Conference on Computer Vision and Pattern Recognition, 1997, pp. 1067–1073.
- [28] Y. Chuang, *A Bayesian Approach to Digital Matting*, In Conference on Computer Vision and Pattern Recognition (CVPR), vol.11, 264-271, 2001.
- [29] Dongbo Min Donghyun Kim Kwanghoon Sohn , *Virtual View Rendering System for 3DTV*, 3DTV Conference: The True Vision - Capture, Transmission and Display of 3D Video, 2008
- [30] A. Smolić, K. Mueller, P. Merkle, T. Rein, M. Kautzner, P. Eisert, and T. Wiegand, Representation, coding, and rendering of 3D video objects with MPEG-4 and H.264/AVC, *Multimedia Signal Processing*, 2004 IEEE 6th Workshop on, 29 Sept.-1 Oct. 2004, p. 379- 382
- [31] Martin A. Fischler and Robert C. Bolles (June 1981), *Random Sample Consensus: A Paradigm for Model Fitting with Applications to Image Analysis and Automated Cartography*, Comm. of the ACM 24: 381–395
- [32] C. Yang, R. Duraiswami, D. DeMenthon and L. Davis. *Mean-Shift Analysis Using Quasi-Newton Methods*, In *IEEE International Conference on Image Processing*, pages 447 - 450, vol.3, 2003.
- [33] P.A. Redert (J. Biemond and E.A. Hendriks thesis advisors), *Multi-Viewpoint Systems for 3D Visual Communication*, Ph.D. thesis, ISBN 90-901-3985-0, pp. 241, October 2000.
- [34] A. M. Eskicioglu, *Application of multidimensional quality measures to reconstructed medical images*, Opt. Eng. 35(3), 778–785 (1996).

- [35] A. M. Eskicioglu, P. S. Fisher, *Image quality measures and their performance*, IEEE Trans. Commun. 43(12), 2959–2965 (1995).
- [36] H. de Ridder, *Minkowsky metrics as a combination rule for digital image coding impairments*, in Human Vision, Visual Processing, and Digital Display III, Proc. SPIE 1666, 17–27 (1992).
- [37] M. Miyahara, K. Kotani, and V. R. Algazi, *Objective picture quality scale (PQS) for image coding* IEEE Trans. Commun. 46~9!, 1213– 1226 (1998).
- [38] N. B. Nill and B. H. Bouzas, *Objective image quality measure derived from digital image power spectra*, Opt. Eng. 31(4), 813–825 (1992).
- [39] P. Franti, *Blockwise distortion measure for statistical and structural errors in digital images*, Signal Process. Image Commun. 13, 89–98 (1998)
- [40] S. Winkler, *A perceptual distortion metric for digital color images*, in Proc. 5th Int. Conf. on Image Processing, Vol. 3, pp. 399–403, Chicago, IL (1998).
- [41] S. Daly, *The visible differences predictor: An algorithm for the assessment of image fidelity*, in Digital Images and Human Vision, edited by A. B. Watson, pp. 179–205, MIT Press, Cambridge, MA (1993).
- [42] T. Frese, C. A. Bouman, and J. P. Allebach, *Methodology for designing image similarity metrics based on human visual system models*, Proc. SPIE /IS&T Conf. on Human Vision and Electronic Imaging II, 3016, 472–483 (1997).
- [43] H.T.Yalazan, M.D.Yucel, *A New Objective Fidelity Criterion for Image Processing: Derivative SNR*, Proc.7'th Mediterranean Electrotechnical Conference - Melecon'94, Vol.1, pp.231-233, Antalya, Turkey, April 1994.
- [44] Fukunaga, Keinosuke; Larry D. Hostetler (January 1975). *The Estimation of the Gradient of a Density Function, with Applications in Pattern Recognition*, IEEE Transactions on Information Theory 21 (1): 32–40. IEEE.
- [45] D. Comaniciu, P. Meer, *Mean shift: A robust approach toward feature space analysis*, IEEE Trans. Pattern Anal. Machine Intell., 24:603–619, 2002.